

# The Star Formation Reference Survey. IV.

## Stellar mass distribution of local star-forming galaxies

P. Bonfini<sup>1,2,3,4★</sup>, A. Zezas<sup>1,2,5</sup>, M. L. N. Ashby<sup>5</sup>, S. P. Willner<sup>5</sup>, A. Maragkoudakis<sup>1,2,6</sup>, K. Kouroumpatzakis<sup>1,2</sup>, P. H. Sell<sup>1,2,7</sup>, and K. Kovalakas<sup>1,2</sup>

<sup>1</sup>Department of Physics, University of Crete, 70013 Heraklion, Crete, Greece

<sup>2</sup>Foundation for Research and Technology-Hellas, 71110 Heraklion, Crete, Greece

<sup>3</sup>Institute for Astronomy, Astrophysics, Space Applications & Remote Sensing, National Observatory of Athens, GR-15236, Penteli, Greece

<sup>4</sup>Computer Science Department, University of Crete, 70013 Heraklion, Crete, Greece

<sup>5</sup>Center for Astrophysics | Harvard & Smithsonian, 60 Garden Street, Cambridge, MA 02138, USA

<sup>6</sup>Western University, 1151 Richmond Street, London, Ontario, N6A 3K7, Canada

<sup>7</sup>Department of Astronomy, Bryant Space Science Center, University of Florida, Gainesville FL 32611, USA

Published in MNRAS 504, 3831–3861 (2021)

### ABSTRACT

We constrain the mass distribution in nearby, star-forming galaxies with the Star Formation Reference Survey (SFRS), a galaxy sample constructed to be representative of all known combinations of star formation rate (SFR), dust temperature, and specific star formation rate (sSFR) that exist in the Local Universe. An innovative two-dimensional bulge/disk decomposition of the 2MASS/ $K_s$ -band images of the SFRS galaxies yields global luminosity and stellar mass functions, along with separate mass functions for their bulges and disks. These accurate mass functions cover the full range from dwarf galaxies to large spirals, and are representative of star-forming galaxies selected based on their infra-red luminosity, unbiased by AGN content and environment. We measure an integrated luminosity density  $j = 1.72 \pm 0.93 \times 10^9 L_{\odot} h^{-1} \text{Mpc}^{-3}$  and a total stellar mass density  $\rho_M = 4.61 \pm 2.40 \times 10^8 M_{\odot} h^{-1} \text{Mpc}^{-3}$ . While the stellar mass of the *average* star-forming galaxy is equally distributed between its sub-components, disks globally dominate the mass density budget by a ratio 4:1 with respect to bulges. In particular, our functions suggest that recent star formation happened primarily in massive systems, where they have yielded a disk stellar mass density larger than that of bulges by more than 1 dex. Our results constitute a reference benchmark for models addressing the assembly of stellar mass on the bulges and disks of local ( $z = 0$ ) star-forming galaxies.

**Key words:** galaxies: evolution — galaxies: luminosity function, mass function — galaxies: photometry — galaxies: star formation — galaxies: structure

## 1 INTRODUCTION

Although there is strong evidence that galaxies generally build their mass in a hierarchical bottom-up sequence, in which smaller units merge to form more massive systems (e.g., White & Rees 1978; Springel et al. 2005; Hopkins et al. 2006; Naab, Johansson, & Ostriker 2009; Hopkins et al. 2010, and references therein), several processes may influence the later stages of the evolution of a galaxy (since  $z \sim 2$ ). For example, a gas-rich object may lose its gas due to a variety of stripping phenomena (e.g., Mayer et al. 2006; Yagi et al. 2010; Brown et al. 2017), while an old galaxy can be rejuvenated by the creation of a new disk from infalling gas (e.g., Steinmetz & Navarro 2002; Marino et al. 2011; Serra et al. 2014). Different models have been recently proposed in order to explain the evolution

of galaxies after  $z \sim 1$  in a comprehensive way, such as the inside-out growth of “red nugget” seeds (Damjanov et al. 2009) or the two-stage formation model, in which an early in-situ star-formation via dissipative processes is followed by accretion of stars formed outside the galaxy (Oser et al. 2010; Driver et al. 2013; Naab 2013).

Any successful galaxy-formation model must at minimum predict local observed galaxy mass functions, the separate mass functions of bulges and disks, the colors of these components, and the dependence of star formation rate (SFR) on stellar mass. The only solid point is the scaling of SFR with mass (a relation commonly referred to as “main sequence of star-forming galaxies”; e.g., Elbaz et al. 2011), for which there is growing evidence against its dependence on the environment, at least since  $z \sim 2$  (e.g., Koyama et al. 2013).

The present work addresses bulge and disk mass functions and the dependence of star formation activity on the stellar mass,

★ E-mail: paolo@physics.uoc.gr

which can itself be interpretable as the integrated product of past star formation. In particular, we constrain the stellar mass function of star-forming galaxies in the Local Universe. Our analysis is based on a representative sample of nearby star-forming galaxies depicting arguably all the star formation phenomenologies and 'blind' to the environment and to AGN content: the Star Formation Reference Survey (SFRS; Ashby et al. 2011). This paper describes the bulge/disk decomposition of the SFRS galaxies, which we use to derive their mass functions as well as the separate mass functions of their disk and bulge sub-components.

This paper is organized as follows. §2 introduces the SFRS project and its aims. §3 presents the  $K$ -band data used for the current study. §4 through §6 describe the procedure to calculate the individual bulge and disk masses; in particular: §4 presents the surface brightness fitting pipeline; §5 presents the decisional algorithm to identify the best-fitting model, while §6 discusses the bulge/disk decomposition. §7 presents the luminosity and stellar mass function for our representative sample of star-forming galaxies as well as the mass functions for their separate bulge and disk sub-components. §8 discusses our results in the context of the current galaxy evolution scheme, and, finally, §9 summarizes our work and conclusions.

Throughout the paper, we assume a flat ( $k = 0$ )  $\Lambda$ CDM cosmology with  $H_0 = 73 \text{ km s}^{-1} \text{ Mpc}^{-1}$  ( $h = H_0/100 = 0.73$ ),  $\Omega_m = 0.3$ ,  $\Lambda_0 = 0.70$ , and  $q = -0.55$ , consistently with Ashby et al. (2011). The quoted  $K$ -band magnitudes refer to the Vega system. The SDSS magnitudes are reported in the native SDSS "maggy" system, very close to the AB system. All the masses reported in this paper are stellar-only, i.e., they do not account for gas nor dark matter, and are based on a Salpeter IMF.

## 2 THE STAR FORMATION REFERENCE SURVEY (SFRS)

This work is based on the Star Formation Reference Survey (SFRS) galaxy sample. The SFRS is designed to determine the conditions under which different star formation estimators are valid. For this reason, 1) it is based on a galaxy sample that is fully representative of all conditions under which star formation is known to take place in the Local Universe, and 2) it assembles as many different star formation tracers as possible for the entire sample (Kouroumpatzakis et al. 2020; Mahajan, et al. 2019). The SFRS sample is drawn from the IRAS PSCz (Saunders et al. 2000), a catalogue of 18 351 objects virtually complete down to its detection limit (0.6 Jy in the IRAS 60  $\mu\text{m}$  band; Figure 1). Because most PSCz galaxies lie within 180 Mpc, the PSCz can be considered an essentially complete catalogue of nearby star-forming galaxies.

In order to include representative numbers of all types of star forming galaxies known to exist in the Local Universe, the SFRS sample was assembled with reference to proxies for dust temperature, SFR, and specific SFR (sSFR; i.e., the SFR per unit stellar mass). This was achieved by sampling the three-dimensional parameter space defined by our adopted proxies — these are:  $F_{100}/F_{60}$ , IRAS 60  $\mu\text{m}$  luminosity, and  $F_{60}/K_s$ . Here  $F_{60}$  and  $F_{100}$  are the flux densities in the two longest-wavelength IRAS bands, and  $K_s$  is the 2MASS  $K_s$ -band flux density, which effectively traces stellar mass. Figure 2 shows how the SFRS galaxies distribute in the 3D parameter space. Further details on the sample creation can be found in Ashby et al. (2011).

In practice, the SFRS selection scheme created a study sample of bright galaxies which is of manageable size without sacrificing the dynamic range of the parent sample. Ultimately, SFRS consists

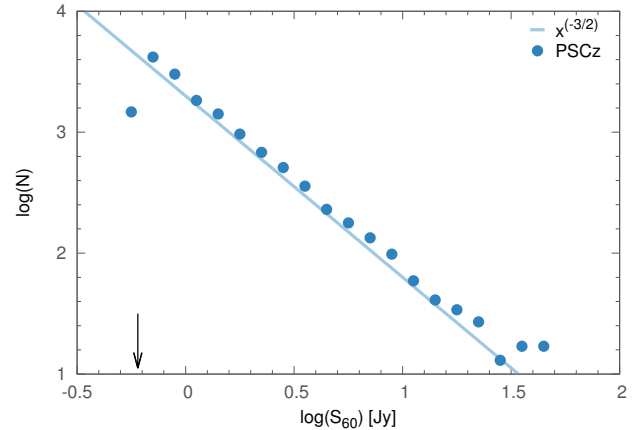


**Figure 1.**  $\log(N)$ - $\log(S_{60})$  distribution of the PSCz sources (data points). The slope of the solid line corresponds to what is expected from a uniform distribution of sources in an Euclidean space ( $N(\text{flux}) \sim S^{-(3/2)}$ ); in this figure, its normalization is arbitrary. The data follow the slope of the Euclidean distribution down to the detection limit of PSCz (0.6 Jy; black arrow), indicating that the catalogue is complete to this flux limit.

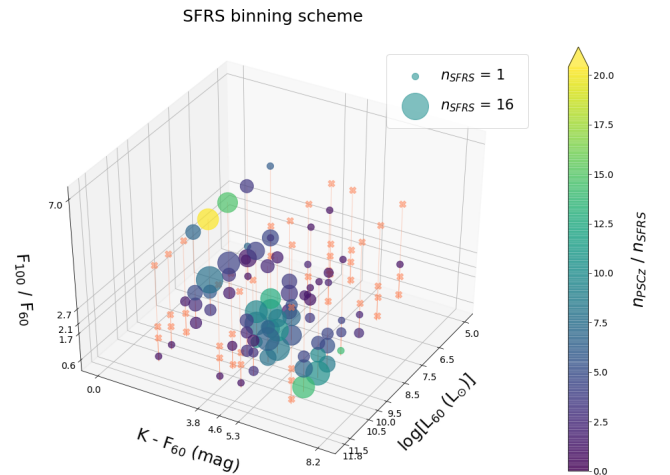


**Figure 2.** Grid of the three-dimensional binning scheme used for the selection of the SFRS sample out of the PSCz catalogue (Ashby et al. 2011). The size of each data point is proportional to the number of SFRS galaxies in that 3D bin. The data color shows the ratio of the PSCz galaxies over the number of SFRS galaxies in the same bin. Empty bins — i.e., potentially populated by PSCz objects but not by SFRS galaxies — are indicated by a cross.

of 369 galaxies spanning 5 orders of magnitude in FIR luminosity and more than 2 orders of magnitude in sSFR. The sampling of galaxies within the aforementioned parameter space allows characterizing star formation activity with respect to the three properties simultaneously without imposing a threshold on any of them. Additionally, there exists a complete classification of the nuclear activity of the SFRS galaxies (Maragkoudakis et al. 2018, see §5), so that the presence of any AGN can be accounted for. In summary, the relative small size of the SFRS sample, coupled with its extensive data sets, allows to perform *detailed* analysis while still fully representing the larger population of star-forming galaxies.

The basic data for the SFRS galaxies are presented in Table 2

of Ashby et al. (2011). When available, the distances were retrieved from the catalogue by Tully et al. (2008), which reports redshift-independent measurements for 127 SFRS objects. For the remaining 242 galaxies, the distances were calculated using the PSC<sub>z</sub> heliocentric velocities, corrected for the gravitational influence of Virgo, the Great Attractor and the Shapley supercluster, according to the prescriptions by Mould et al. (2000).

### 3 K-BAND DATA

In order to investigate the relation between star formation and galaxy stellar mass and morphology, we first separated the contributions of the bulge and disk components to the total stellar mass of each SFRS galaxy. The stellar mass of a galaxy is best described by its emission in the *K*-band, which is largely dominated by the contribution of main sequence and giant long-lived stars (e.g., Binney & Tremaine 1987) and is minimally affected by the absorption by the interstellar medium (Devereux, Becklin, & Scoville 1987). Young, massive stars are relatively minor contributors to galaxies' *K*-band emission. Although those objects significantly affect the optical emission of a late-type galaxy (for stars along the main sequence  $L \propto M^{3.5}$ ), they do not play a significant role in the mass balance of a galaxy, due to their relatively short lives and low number density (e.g., Binney & Tremaine 1987).

To measure the stellar components, we obtained 2MASS All Sky Survey *K<sub>s</sub>*-band images for the SFRS sources, on which we performed photometry based on the total light derived by modelling their surface brightness. The results were then used to calculate the total stellar mass of each galaxy as well as the stellar mass of its disk and bulge sub-components when this was possible.

#### 3.1 The 2MASS Extended Source Catalogue photometry

The 2MASS Extended Source Catalog (2MASS-XSC; Jarrett et al. 2000) is 90% complete down to  $K = 13.5$  mag and provides uniform coverage of our target galaxies. This catalogue does not provide information for the disk/bulge sub-components, but it will be used, in this paper, as a comparison for the integrated magnitudes. The 2MASS-XSC essentially offers 2 kinds of extended fluxes, which correspond to aperture photometry within the “Kron” and the “total” radii, respectively. The former is derived from the intensity-weighted first-moment radius (e.g., Bertin & Arnouts 1996), while the latter is derived by means of a curve-of-growth technique.

While the Kron radius is known to exclude a small (few percent) but constant fraction of the flux, independently of the object magnitude (e.g., Kron 1980), the so-called “total” (extrapolated) magnitudes recover most of the flux from the source and were therefore selected as a comparison benchmark for the total luminosities derived in our work. The extrapolated *K<sub>s</sub>*-band magnitudes for all the SFRS targets are reported in Table D1, along with the corresponding *J*-band and *H*-band magnitudes. For ~10 objects, no 2MASS-XSC counterparts were identified due to the small angular size of the targets. For these galaxies we report instead the magnitudes of the corresponding 2MASS Point Source Catalogue (2MASS-PSC) counterparts, which we identified visually.

Both the Kron and total apertures are affected by several major issues. In fact, the definition of both apertures in 2MASS relies on a Sérsic fit to the surface brightness profile of the galaxies between 5'' (a radial distance considered out of the PSF influence) and the radius

where the *S/N* falls below 2<sup>1</sup>. Not only may a single Sérsic model be an over-simplification of the light profile, but also, due to the modest average exposure times of the combined 2MASS mosaics (7.8 sec; §3.2), the *S/N* ~ 2 threshold may constrain the Sérsic fit only within a very small galactocentric radial range and in turn yield an erroneous Kron/total radius. Secondly, there is no certainty that the flux within the apertures won't include a contribution by the background. Finally, contaminating objects (mainly stars) may fall within the aperture and contribute to the source flux if the automated masking did not work properly due to source blending. There is growing evidence that the 2MASS photometry is affected by systematic biases which lead to severely underestimated (10% to 40%) isophotal and total luminosities (e.g., Andreon 2002; Kirby et al. 2008; Schombert 2011), even for bright ellipticals.

Our modelling of the light profiles of the galaxies (presented in §4), which is primarily intended to perform disk/bulge decomposition, also largely overcomes the limitations of the 2MASS apertures by accurately evaluating the background component, by accounting for the extended wings of the surface brightness profiles of the sources, and by carefully masking foreground stars and contaminating objects.

#### 3.2 The 2MASS data for the SFRS targets

The 2MASS observational strategy mapped each piece of the surveyed area with overlapping tiles (Beichman et al. 1998), where each tile covers a projected area in the sky of 6° × 8'.5. The main 2MASS scientific image products are the “Atlas” (or “co-add”) images, which were produced by the combination of 6 frames and have a size of 512 × 1024 pixels, for an exposure time of 7.8 s at each sky location. In the combination process, the original pixel scale (2''/pixel) is resampled to 1''/pixel, so that the area covered by an Atlas image is 8'.5 × 17'.

As part of the star-galaxy discrimination process, the 2MASS pipeline also created “postage-stamp” images for each of the extended sources detected in the co-add images. The postage-stamps were conservatively cropped from the Atlas images around the target of interest, for a size which is a multiple of the Kron radius of the source, so as to not miss any galactic light. Despite the obvious advantage of dealing with source-specific images, we preferred the larger Atlas products, because — for calibration purposes (see §4) — we wanted to include as many field stars as possible and have an independent estimation of the local background. We retrieved 2MASS *K<sub>s</sub>*-band Atlas images for all the SFRS sources from the NASA-IPAC Infrared Science Archive.

## 4 THE 2D FIT OF SFRS GALAXIES

The core of our analysis was our derivation of separate disk and bulge luminosities and masses, based on innovative two-dimensional (2D) fitting to the *K<sub>s</sub>*-band surface brightness in 2MASS *K<sub>s</sub>* Atlas images of the SFRS galaxies. These luminosities were then used to estimate the bulge and disk masses. Out of the 369 SFRS targets, we excluded from this analysis 19 interacting galaxies with strongly disturbed morphologies, for which the definition of “bulge” or “disk” is ambiguous and whose surface brightness distribution cannot be represented with a parametric function.

<sup>1</sup> For more details on the definition of the 2MASS apertures, refer to the 2MASS documentation or Jarrett et al. (2000)

Nonetheless, these galaxies are included in the determination of the integrated galaxy mass function (see §7.6). Moreover, we excluded 5 targets which host a dominant AGN and which appear as point-like sources in the 2MASS data. Therefore, the actual sample we will consider hereafter is composed of 345 galaxies.

There are a number of available tools for the 2D fit of astronomical images, of which the most widely used are arguably GIM2D (Simard 1998) and GALFIT (Peng et al. 2010). In their testing review, Häussler et al. (2007) discussed the treatment of the uncertainties of the two codes and their robustness in crowded-field environments. They concluded that GALFIT has an advantage in terms of dealing with contaminating objects (which can be fit independently), although both codes underestimate uncertainties in the fitted parameters. For our analysis, we therefore opted to use GALFIT v.3<sup>2</sup>. This version of GALFIT implements the possibility of fitting complex and asymmetric galaxy features such as spiral arms, rings, bars, etc. via Fourier modification of standard models (exponential disk, Sérsic, etc.) or coordinate rotations along the radial direction. Although extremely appealing, we decided not to make use of these new features, because — as they are currently implemented — they are mostly based on the observer’s interpretation and because the quality of the 2MASS data generally did not allow such level of detailed modelling.

Due to the relatively large number of targets (345), the variety of morphological models we intended to apply, and the preparatory steps (e.g., PSF creation, object masking, etc.), we created a fully-automated pipeline based on GALFIT to perform the 2D fits. The resulting code is flexible and with minor changes can be adapted to different types of data, given that it essentially requires as input just an estimate of the point-spread-function (PSF) FWHM ( $\text{FWHM}_{PSF}$ ) and a list of target positions.

#### 4.1 Fit procedure

Our fitting pipeline operates according to the following procedure:

- 1) it sets up GALFIT input files and first-guess parameters
- 2) it creates masks for the contaminating objects
- 3) it creates the PSF used for the model convolution
- 4) it fits the targets with different parametric models:
  - 4a— it first fits a simple Sérsic function
  - 4b— it uses the results as input parameters for the next step
  - 4c— it fits nested disk, bulge, and AGN components
- 5) it calculates the magnitude zero-point
- 6) it converts integrated luminosities into masses

The details of the preparatory steps 1, 2, and 3 are reported in Appendix A, while the calibration steps 5 and 6 are presented in Appendix B; in the remainder of this section we will focus instead on the fitting process.

The fit procedure itself consisted of multiple steps. First, we fitted all the objects using the Sérsic function, with the following variants:

- Sérsic model with free Sérsic index  $n$  (Sérsic)
- Sérsic model with fixed Sérsic index  $n = 1$  (Sérsic <sup>$n=1$</sup> )
- Sérsic model with fixed Sérsic index  $n = 4$  (Sérsic <sup>$n=4$</sup> )

We introduced the Sérsic models with fixed index (i.e., Sérsic <sup>$n=1$</sup> , and Sérsic <sup>$n=4$</sup> ) in order to reduce the number of degrees of freedom and assist the fit of problematic targets for which the free-index

<sup>2</sup> <http://users.obs.carnegiescience.edu/peng/work/galfit/galfit.html>

GALFIT SÉRSIC PARAMETERS			
Parameter	Sérsic	Sérsic <sup><math>n=1</math></sup>	Sérsic <sup><math>n=4</math></sup>
(1)	(2)	(3)	(4)
CENTER (X,Y)	○	○	○
MAGNITUDE	○	○	○
$R_e$	○	○	○
AXIS RATIO	○	○	○
P.A.	○	○	○
SÉRSIC $n$	○	●	●
BOXINESS	●	●	●

**Table 1.** Free/fixed parameters for the Sérsic models. (1) Parameter type. (2) (3) (4) The ○ and ● symbols indicate free and fixed parameters, respectively, for the Sérsic, Sérsic <sup>$n=1$</sup> , and Sérsic <sup>$n=4$</sup>  models.

Sérsic fit failed. Apart from the Sérsic indices, we allowed all other model parameters to vary, except for the “boxiness” (or “diskyness”). This parameter gives a measure of the deviation from a perfect elliptical shape, a feature routinely observed in the isophotes of galaxies throughout the whole Hubble sequence (see Ciambur 2016 for a mathematical description of isophote shapes). However, a second order parameter such as the boxiness is not realistically quantifiable for the vast majority of our sample galaxies, whose effective radii are just a few pixels on the 2MASS images (or just over the PSF size). On the contrary, we observed that galaxies with low bulge to disk ratios were erroneously reproduced by extremely disky models with a single component if the parameter was left free to vary. Given the limitations of our data, we therefore decided to fix this parameter to the value of 1 (i.e., no boxiness) for the current analysis. The list of “frozen”/“thawed” parameters for the different Sérsic models is summarized in Table 1.

In each fit, we also included a constant to fit the sky background, whose value was derived as discussed in Appendix A1. Although GALFIT offers the possibility to add a “gradient” parameter to the sky model, we preferred not to complicate the fit by adding this extra degree of freedom, because: *a*) we might introduce degeneracies with the parameters of the galaxy models (see discussion in Appendix A1), *b*) we already limited any large-scale background variation by considering a fit region specifically cropped around each source, and *c*) the  $K_s$ -band background of the 2MASS images (which is due to thermal continuum) in standard observational conditions does not present high-frequency structures (as it often happens for the  $J$  and  $H$ -bands).

GALFIT is based on a least-squares minimization; the fit statistic of  $\chi^2$  is defined as:

$$\chi^2 = \sum_{x=1}^{nx} \sum_{y=1}^{ny} \frac{(f_{data}(x,y) - f_{model}(x,y))^2}{\sigma(x,y)^2} \quad (1)$$

where  $f_{data}(x,y)$  are the counts of the  $(x,y)$  pixel of the input image,  $f_{model}(x,y)$  are the counts of the corresponding pixel in the PSF-convolved model image generated at each iteration,  $x$  and  $y$  refer to the pixels in the images, and  $\sigma(x,y)$  is the uncertainty or “sigma” image. The sigma image is used to weight the discrepancy of the model to the data, given the statistical uncertainty of the observed counts of each pixel, and it is calculated internally by GALFIT. The  $1-\sigma$  errors are calculated for all free parameters based on their fit covariance matrix (Peng et al. 2010). As an intuitive indicator of the goodness of fit we adopted the *reduced*  $\chi^2$  ( $\chi^2_{red}$ ), defined as the  $\chi^2$  divided by the number of degrees of freedom ( $N_{DOF}$ ), i.e.:



$$\chi_V^2 = \frac{\chi^2}{N_{\text{DOF}}} \quad (2)$$

We set some mild constraints on the fit parameters and in particular on the Sérsic index, the effective radius, and, most importantly, on the model total magnitude, having found GALFIT particularly sensitive to this parameter. These limits were based on the initial results from the SExtractor run on each field (Appendix A2), and they were imposed in order to minimize the possibility of a failed or wrong fit rather than to actually constrain the fit. In fact, all the models which hit the parameter limits were attributed an arbitrarily large magnitude error and were rejected by the magnitude criterion imposed in the process of *best-fit* model selection (§5). Additionally, we constrained the positions of contaminating objects (within about  $\pm 1$  FWHM<sub>PSF</sub>) to avoid large shifts of their centers during the fit, which would result in their taking the place of a sub-component of the main target.

Contaminating objects were fit with different models, based on their spatial extent: small, quasi point-like sources were fit with a Gaussian model, while for the extended ones we adopted a Sérsic model. Small objects were distinguished from extended ones based on their effective radius ( $R_e$ ) as calculated by SExtractor, with the separating threshold set at  $R_e = 1.5 \times \text{FWHM}_{\text{PSF}}$ .

We used the results of the single Sérsic fits as first-guess parameters to implement more complex models, intended to separately account for different galaxy components. In particular, we wanted to model bulges and disks with Sérsic and exponential (exDisk) profiles respectively, and AGNs with a PSF component. The evaluation of the fit results, and the disk/bulge separation procedure based on them will be presented in Section 5. These additional, more complex models were:

- ▶ Sérsic + PSF (Sérsic + psfAgn)
- ▶ Sérsic + exponential disk (Sérsic + exDisk)
- ▶ Sérsic + exponential disk + PSF (Sérsic + exDisk + psfAgn)

An accurate estimate of the first-guess input magnitude of each model component turned out to be critical to guarantee the convergence of these fits. We calculated the brightness of each component by re-distributing the integrated flux of the Sérsic model obtained above: in the case of Sérsic + psfAgn, the PSF component was initially attributed 1/10 of the total flux; in the other cases the flux was re-distributed equally among the components.

At this stage, the constraints for the contaminating objects were simply inherited from the previous Sérsic run. For the targets of interest, we instead imposed new, stricter rules, given that we could now rely on the first-guess parameters from the *best-fit* Sérsic models. In particular, we enforced that: *a*) the centres of all the components (either Sérsic, exDisk, or psfAgn) associated to a target were locked within a range of  $\pm 1/2$  FWHM<sub>PSF</sub>, and *b*) the effective radius of a disk should be at least 20% more than that of the associated bulge. The latter measure ensured that the bulge component, as we physically interpret it, was automatically contained within the disk component. By imposing this, we of course ignore embedded disks: those features are not expected to be observable in the few early-type galaxies in our sample, given the poor 2MASS resolution (§3.2).

Figure 3 illustrates our fitting procedure for one typical galaxy, UGC 6625. The fit statistics for each model of UGC 6625 are reported in Table 2. This specific target contains an AGN (see Table D2), and the *best-fit* model turned out to be Sérsic + psfAgn + exDisk. Figure 3 highlights how difficult it is to distinguish by eye the *best-fit* model, especially because models with more components

FIT RESULTS FOR UGC 6625		
Model	$\chi_V^2$	$\sigma_{\chi_S}^2$
(1)	(2)	(3)
Sérsic	1.141	1.451 (0.111)
Sérsic + psfAgn	1.136	1.185 (0.103)
Sérsic + exDisk	1.142	1.608 (0.116)
Sérsic + psfAgn + exDisk	1.136	1.325 (0.107)

**Table 2.** Statistical results of the GALFIT fits to the object UGC 6625, for the models shown in Figure 3.

(1) Fit model. (2) Reduced  $\chi^2$ . (3) Excess variance (described in Section 5).

will automatically yield better residuals without necessarily providing a statistically significant improvement of the fit (i.e., without being more representative). Our model selection procedure, designed to overcome this issue, is described in §5.

## 5 BEST-FIT MODEL SELECTION

For each of the 345 SFRS galaxies composing our sample, our pipeline attempted a fit using all of the following models (see §4.1):

- ▶ Sérsic model with free index  $n$  (Sérsic)
- ▶ Sérsic model with fixed index  $n = 1$  (Sérsic <sup>$n=1$</sup> )
- ▶ Sérsic model with fixed index  $n = 4$  (Sérsic <sup>$n=4$</sup> )
- ▶ Sérsic + PSF (Sérsic + psfAgn)
- ▶ Sérsic + exponential disk (Sérsic + exDisk)
- ▶ Sérsic + exponential disk + PSF (Sérsic + exDisk + psfAgn)

Not all of the fits were necessarily successful for each of the targets, meaning that in some cases GALFIT did not converge (hence providing unreliable parameter values) or it crashed due to any of the parameters exceeding the hard-coded thresholds. Actually, for 3 objects we could not obtain any fit with the aforementioned models. These galaxies are OJ 287, IRAS 13218+0552, and IRAS 11069+2711: a visual inspection of their 2MASS images revealed that these objects are only marginally resolved, hence not allowing any meaningful spatial fit. For an additional 7 galaxies, the recovered magnitudes from all the models differed by more than 1 mag from the corresponding 2MASS counterpart (see below). These are galaxies affected by severe contamination by neighbouring objects, an issue which is properly accounted for in our routines but not in the 2MASS pipelines. For a robust consistency check with the 2MASS catalogue we discarded the above 7 galaxies (accounting for only ~3% of the sample), hence applying our analysis to the remaining 335 objects.

Among the valid, successful fits (which often had very similar  $\chi_V^2$  and residual patterns; see e.g., Table 2 and Figure 3), we had to determine the “best-model” (i.e., the most appropriate among the *best-fits* of the 6 models presented above). The selected model automatically defines the separation of any bulge or disk component of the galaxy (see §6). Therefore, the selection procedure had to take into account both the fit results and morphological considerations.

The selection sequence we applied to determine the best-model from the original pool of models was.

- 1) *Rejection of unphysical results* — Figure 4 compares the 2MASS  $K_s$ -band magnitudes against those computed by GALFIT. There is, in general, good agreement between the 2MASS and the GALFIT data, although a few models present (often at the same time) two kinds of suspect behaviours: (1) unrealistically large

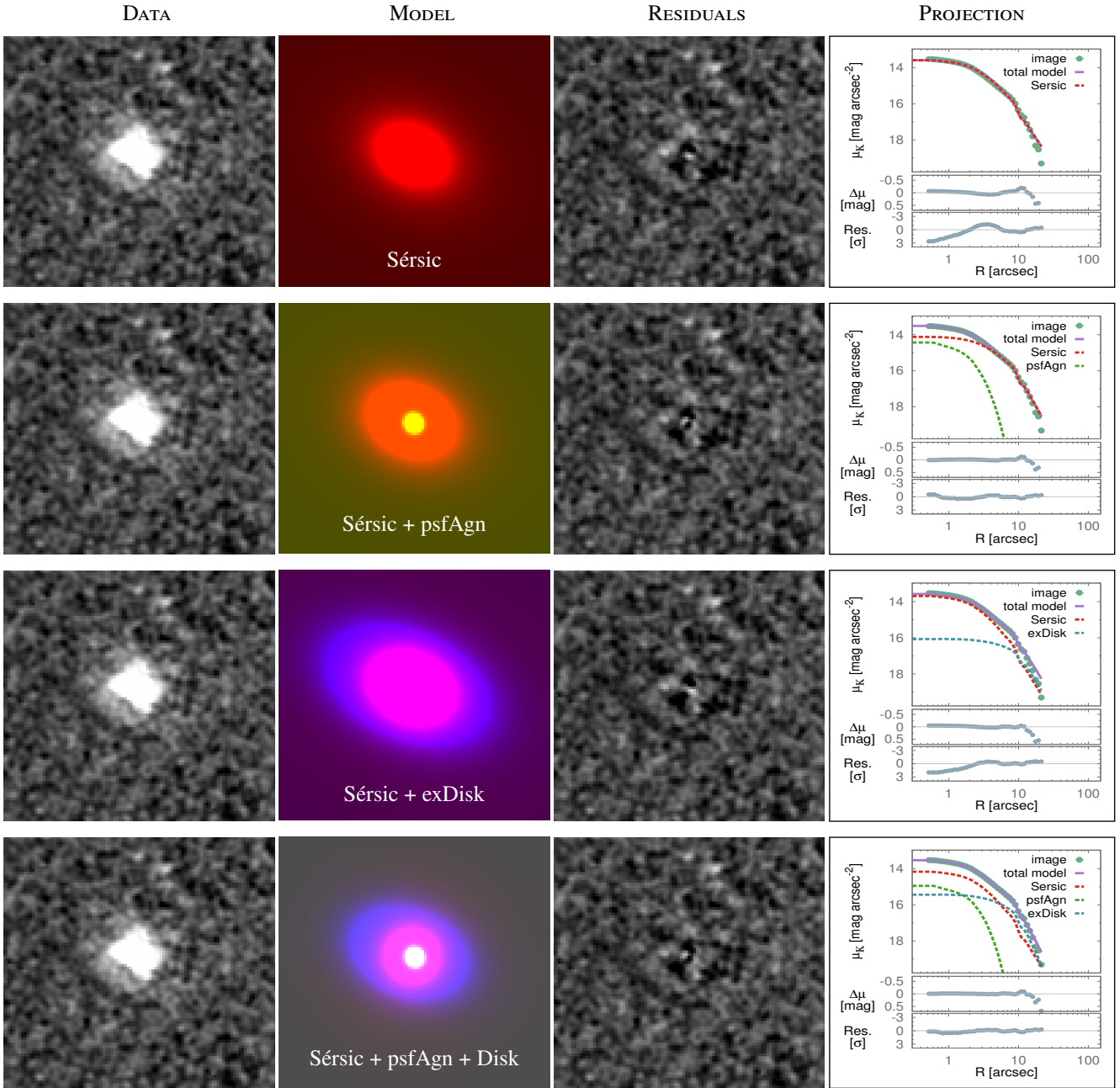


**Figure 3.** Results of the fits for the object UGC 6625, performed using the models presented in §4.1. The first, second, and third columns from the left show the data, model, and residuals, respectively, for the (from top to bottom) Sérsic, Sérsic + psfAgn, Sérsic + exDisk, and Sérsic + psfAgn + exDisk models. The model images (center-left) are arbitrarily color-coded in order to highlight the separate Sérsic (red), psfAgn (green), and exDisk (blue) components and to show their relative intensity, extension, and centres. The right-hand column shows one-dimensional radial projections of the data, models, and residuals along concentric isophotes: the image data are shown in green, the total model is shown with a violet line, and its sub-components with dashed lines coloured according to the same scheme as for the model image. We stress that the curves in the plots do *not* represent the “standard” fits to the major-axis surface brightnesses but are rather 1D radial projections of the separate 2D images. These radial projections were obtained with the technique described in Bonfini, Dullo, & Graham (2015). In brief: we first measured the galaxian surface brightness along the elliptical isophotes identified on the data image by the IRAF.ellipse task (Jedrzejewski 1987); then, we obtained the radial profiles from the images of the 2D model (for the individual sub-components as well as their sum, i.e., the total emission) by measuring their surface brightnesses over exactly the same isophotes. Finally, the two lower panels of each plot present the projections of the residuals (gray points), first expressed in terms of mag/arcsec $^2$ , and then in terms of data noise ( $\sigma$ ). For this specific target, the *best-fit* model (selected as described in §5) is the Sérsic + psfAgn + exDisk. For this object we can ignore the Sérsic $^{n=1}$  and Sérsic $^{n=4}$  models, because the [free index] Sérsic yielded a successful fit.

uncertainties in their integrated magnitudes<sup>3</sup> compared to the magnitude uncertainties of other model fits to the same target; (2) significant discrepancy with respect to the integrated 2MASS magnitudes. The former issue is related to non-converging fits or numerical issues during the GALFIT iterations, while the latter is due to the presence of contaminating objects (not properly treated by the 2MASS pipeline) or to models not accounting for the central AGN component (see point 2).

Although many of these erroneous results would be rejected in the following steps of our analysis (because they are not trustworthy due to their low statistics; e.g., low  $\chi^2_V$ ), we imposed sharp limits on the magnitude uncertainties ( $\delta M_K < 1$  mag) and on their difference from the 2MASS magnitudes ( $|m_{GALFIT} - m_{2MASS}| < 1$  mag) in order to exclude the most deviant models. The latter margin was based on the scatter of the points on the GALFIT–2MASS comparison (Figure 4) around their best-fit line, and it corresponds to  $\sim 6$  times the average uncertainty of the faintest 2MASS objects. We chose this conservative value in order not to excessively penalize our photometry, which has been performed with higher accuracy than that of 2MASS.

2.a) *Accounting for AGNs* — As mentioned at the beginning of §4, we excluded from our sample any SFRS galaxy unresolved in the 2MASS images and hosting an AGN due to the impossibility of performing a bulge/disk decomposition (namely, we excluded: IC 486, 3C 273, UGC 8058, IRAS 13144+4508, and UGC 8850). However this is not sufficient, because the uncertainty about the presence of an AGN can severely influence the modelled near-IR morphology of a galaxy and in turn cause an incorrect estimation of the galaxy/bulge mass.

When fitting a galaxy hosting a central AGN with a Sérsic + exDisk model, the central Sérsic might account for the AGN by acquiring extreme Sérsic  $n$  and effective radius values (so that the profile effectively resembles a point-like source). When fitting it with a single Sérsic component, the AGN can shift the surface brightness normalization upwards (see point 1) or — as for the previous case — force an unrealistically large Sérsic index. Even a low-luminosity AGN, if overlooked, can still affect the total luminosity budget of a model by e.g., mimicking a bulge component. Conversely, our models including a psfAgn component need to be accurately screened in order to avoid misinterpreting an unresolved bulge (i.e., a PSF) as an AGN.

It is therefore of vital importance to ensure that the point-like AGN component is isolated. To this purpose, we took advantage of the activity classification of the SFRS nuclear sources provided by Maragkoudakis et al. (2018). The activity classification was based on a combination of optical emission line diagnostics (the 3 variations of the BPT diagrams) and IR-colour diagnostics (Stern et al. 2005). In addition, to account for host-galaxy light contamination in the nuclear colours of the galaxies, the authors performed matched aperture photometry to the nuclear regions of all the IRAC images and designed a “nuclear-color Stern diagram”, which then revealed obscured AGN not identified with the standard integrated IRAC colours Stern plot. The SFRS activity classification consists of: 269 (73%) star-forming galaxies, 50 (13%) Seyferts (Sy; including 3C 273 and OJ 287), 33 (9%) LINERs, and 17 (5%) transition objects (TOs). Because

this classification is based on star-light subtracted spectra it minimizes the effect of dilution of the AGN by the stellar component of the host galaxy (see Maragkoudakis et al. 2014). For the current study, we considered as “secure” AGNs only the 50 SFRS galaxies identified as Seyferts.

For these targets, the models *not* including a psfAgn component were automatically rejected (unless they were the only successful fits). For the remaining objects, we excluded at this stage the Sérsic + psfAgn + exDisk model, but we kept all the others, including the Sérsic + psfAgn (but in this case we assumed that the central PSF represented an unresolved bulge; see §6).

- 2.b) *Accounting for TOs* — Transition objects are defined as sources of composite contribution from both star-forming and AGN activity, falling in between the H II and AGN regions in the [N II]/H $\alpha$  BPT diagram. Maragkoudakis et al. (2018), following the combined classification scheme from all three BPT diagnostics, applied stricter conditions in the definition of TOs. Specifically, a galaxy was assigned a TO classification when all of the following three conditions applied: (i) it was defined as a TO by the [N II]/H $\alpha$  diagnostic; (ii) it was attributed a Sy or LINER classification by one of the other BPTs; and (iii) it was attributed a H II classification by the remaining diagrams. For these objects, if a Sérsic + psfAgn + exDisk model was successful, we ignored the Sérsic + psfAgn one. The reason is that, in TOs, the nuclear component could host contributions from both AGN and star formation emission (Ho, Filippenko, & Sargent 1993). Given the rules set by point 2, adopting the Sérsic + psfAgn model would have implied that *all* the nuclear emission was associated with an AGN. The Sérsic + psfAgn + exDisk model is instead more suitable to redistribute the nuclear emission between star-forming regions and AGN.
- 3) *Evaluation of Sérsic<sup>n=1</sup> and Sérsic<sup>n=4</sup> models* — We introduced the Sérsic models with fixed index (i.e., Sérsic<sup>n=1</sup> and Sérsic<sup>n=4</sup>) only to assist the fit of those  $\sim 10$  problematic targets for which the free-index Sérsic fit failed. Therefore, in case the Sérsic fit with free index was successful, these models were not considered.
- 4) *Selection of model with best statistics* — The statistic minimized by GALFIT in order to converge to the best-fit parameters is the  $\chi^2_V$ . However, this statistic cannot be used as a parameter to decide the best model, given that the models contain a different number of components. In these cases, it is common to adopt the  $F$ -test (e.g., Bevington & Robinson 2003) in order to assess the importance of an additional component (e.g., a bulge or a PSF component), but this test has been shown to be problematic in the case of fits within a bounded parameter space (as in our case where we constrain the range of the model parameters; see e.g., Protassov et al. 2002). We therefore preferred to define a metric based on the residual image, which gives a direct picture of how well a model represents the spatial distribution of the source intensity and accounts for its total flux (which is our goal in this effort).

The absolute value of the sum of the residual counts over the fitted area is not indicative of the quality of the fit. The reason is that a model may be a poor fit but generate an equal amount of positive and negative residual counts, so that the sum is close to 0. A similar argument holds against the average value of the residuals (i.e., the sum of the residuals divided by the area of the fit). A better representation of the deviation of the residuals is given in their RMS variation within the area of the fit. However, one has to consider the RMS of the residuals generated only

<sup>3</sup> Calculated as the sum in quadrature of the uncertainty on the fit magnitude and the zero-point uncertainty.

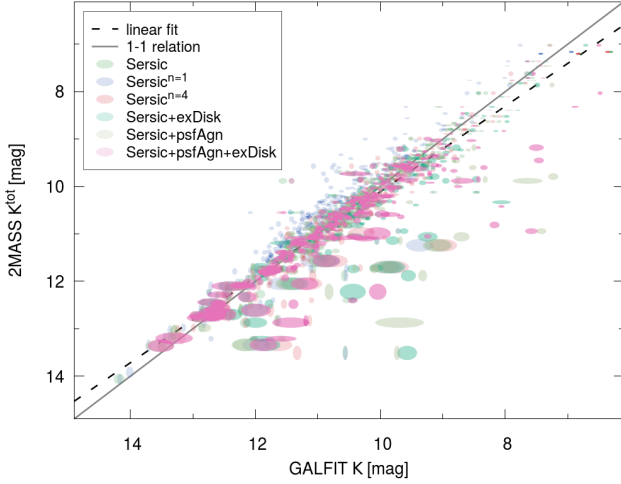


**Figure 4.** Comparison of catalogued 2MASS total magnitudes to those derived by our GALFIT-based fitting procedure described in §4 for all the targets and all the models. The results plotted here refer to all successful fits for all SFRS galaxies (the 6 different models applied to each object are coded by different colors). The sizes of the ellipses represent the statistical uncertainties. The solid line shows the 1-to-1 relation, while the dashed black line is a linear fit to the data.

by the subtraction of the model from the galaxy light profile, excluding the noise due to the fit of the background. Following Vaughan et al. (2003, their equation 8), we defined an *excess variance* statistic:

$$\sigma_{XS}^2 = \sigma_{objects}^2 - \sigma_{sky}^2 \quad (3)$$

where  $\sigma_{objects}$  and  $\sigma_{sky}$  represent the RMS of the residual image evaluated over the fitted target(s) and the sky areas, respectively. This quantity evaluates the amplitude of the variations in the residuals at the area of an object, after removing the statistical variations purely due to the background component (which gives a reference baseline noise in a source-free region). The uncertainty on  $\sigma_{XS}^2$  is given by the same authors (their equation 11), as:

$$\delta\sigma_{XS}^2 = \sqrt{\frac{2}{N_{objects}} \cdot (\sigma_{sky}^2)^2 + \frac{\sigma_{sky}^2}{N_{objects}} \cdot 4\sigma_{XS}^2}, \quad (4)$$

where  $N_{objects}$  is the number of pixels corresponding to the object(s) area. For the cases in which the objects residuals  $\sigma_{objects}$  are close to the background variation ( $\sigma_{objects} \approx \sigma_{sky}^2$ ), Equation 4 simplifies into:

$$\delta\sigma_{XS}^2 = \sqrt{\frac{2}{N_{objects}} \cdot (\sigma_{sky}^2)^2}. \quad (5)$$

To correctly calculate  $\sigma_{objects}$  from the residual image, we used a “negative mask” in which the only valid pixels are those corresponding to the objects of interest. The *center-right* panel of Figure A2 shows the negative mask for NGC 4438: the companion galaxy NGC 4435 (N-W of the target), despite being part of our sample, is masked-out because its fit is performed within a separate region and its residuals must not affect the model selection results for our target of interest. Similarly, to calculate  $\sigma_{sky}$  we adopted a “negative background mask” which hid all the

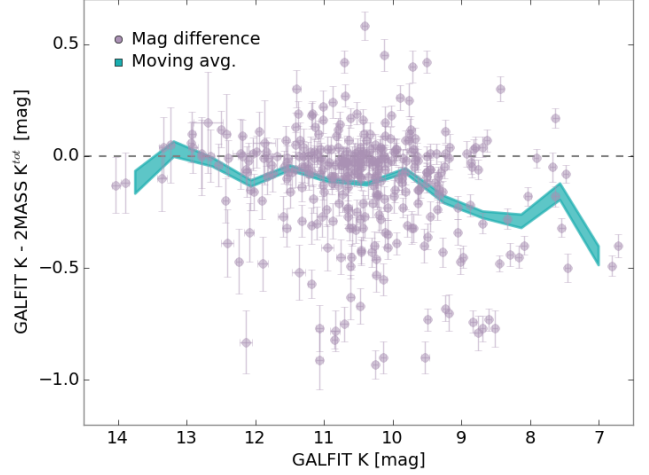


**Figure 5.** Comparison between the 2MASS total magnitudes and the ones computed by GALFIT, for the selected models. The data points represent the magnitude difference as a function of the GALFIT magnitude, while the shaded area shows the moving average (and its uncertainty), which has been evaluated adopting a smoothing box of 0.5 mag in size. The upper and lower bounds of the curve represent the  $1\text{-}\sigma$  width of the distribution of moving averages calculated over 500 mock samples generated by Monte-Carlo sampling the data points within their respective errors.

sources (see e.g., Figure A2, *right* panel)<sup>4</sup>. For each target, we selected the *best-statistic* model as the one having the smallest  $\sigma_{XS}^2$ .

- 5) *Selection of candidate best-models* — In order to account for statistical uncertainties, a pool of additional “good-fit” models with  $\sigma_{XS}^2$  around the *best-statistic* model excess variance ( $\sigma_{XS,best}^2$ ) with a tolerance set by  $\delta\sigma_{XS,best}^2$  was selected.
- 6) *Screening for the simplest models* — The models which “survived” up to this stage were considered equivalent. Given this assumption, there is no reason to prefer a more complex model when a simpler one can give an equally valid interpretation of the data. Therefore, among the surviving models, the simplest models were selected (i.e., the one with fewest number of components). If the surviving models had the same number of components they were all kept. In any case though, given the selection scheme and the composition of the available models (i.e., Sérsic, Sérsic<sup>n=1</sup>, Sérsic<sup>n=4</sup>, Sérsic + psfAgn, etc.), there were no more than 2 models left in the *final* pool.
- 7) *Final choice of best-fit model* — In these few cases with more than one final model, the selected *best-fit* model was the one with the smallest  $\sigma_{XS}^2$  within the *final* pool. Notice that, due to point 6, it did not necessarily correspond to the  $\sigma_{XS,best}^2$  model.

Following the case of the example galaxy UGC 6625 (Figure 3), our routine operated in this way: at point 1, no model was rejected; at point 2, because the nuclear source was classified as TO, the Sérsic + psfAgn model was excluded; at point 3, the Sérsic model being

<sup>4</sup> Notice that this “negative background map” is *not* a reverse of the conservative background mask image described in A1, and used to evaluate the sky statistics. Instead, it is a [roughly] complementary image to the “negative mask” for the object.



successful, the Sérsic<sup>*n*=1</sup> and Sérsic<sup>*n*=4</sup> models were excluded; at point 4, the Sérsic + psfAgn + exDisk model was selected due to the best  $\sigma_{XS}^2$ ; at point 5, no model was added to the pool (being every other model either excluded or having a  $\sigma_{XS}^2$  larger than  $\sigma_{XS}^2 + \sigma_{XS,best}^2$ ), hence prematurely selecting the Sérsic + psfAgn + exDisk combination as the *best-model*. Notice that this model does *not* correspond to the best  $\chi^2_\nu$  nor  $\sigma_{XS}^2$  (see Table 2) because our model selection procedure considers several more criteria.

The summary of our GALFIT fit results, along with the corresponding masses for the *best-models* are reported in Table D2. Figure 5 shows the difference between the 2MASS total magnitudes and the *best-model* ones computed by GALFIT. The 2MASS magnitudes are on average  $0.12 \pm 0.24$  mag fainter than our GALFIT magnitudes. This is consistent with the systematic  $\sim 0.3$  mag underestimation of the catalogued 2MASS magnitudes found by Schombert (2011). Lauer et al. (2007) argue that one possible reason for the underestimation lies in the fact that the 2MASS-XSC calculation of total magnitudes erroneously “assumes that the galaxies essentially have exponential profiles”. This potentially explains why we retrieve a smaller magnitude discrepancy than Schombert (2011). In fact, while their sample is composed of elliptical galaxies, the SFRS objects are predominantly late-type galaxies and hence closer to satisfying the 2MASS-XSC assumption of having pure exponential profiles.

## 6 SEPARATION OF DISK/BULGE COMPONENTS

After the *best-fit* model selection was completed, we proceeded with separating the bulge from the disk components. This was a trivial task in case the *best-fit* model turned out to be the Sérsic + exDisk + psfAgn<sup>5</sup>. In this case the Sérsic component naturally represents the bulge while the exponential component represents the disk, and, if the galaxy hosts a central Seyfert source, the psfAgn component obviously represents the AGN. If instead the central object was spectroscopically classified as TO (i.e., of uncertain nature; see §5), it would be here re-classified as “AGN”. For all the other *best-fit* models, deciding what each component represents was more complicated, as detailed in the following scheme:

- ▶ psfAgn component
  - ↔ considered an “AGN” if the object is known to host a Seyfert or a TO central source
  - ↔ considered a “bulge” otherwise
- ▶ Sérsic component
  - ↔ always considered a “disk” if  $n \leq 1.5^6$
  - or else:
    - ↔ considered a “mixed” component in Sérsic *best-fit* model and, if the object is known to host a Seyfert, also in Sérsic + psfAgn
    - ↔ considered a “disk” in Sérsic + psfAgn *best-fit* model if psfAgn is considered a “bulge”
    - ↔ considered a “bulge” otherwise
- ▶ exDisk component

<sup>5</sup> As mentioned in §5, this model could be selected only if the galaxy hosted a Seyfert or TO central source.

<sup>6</sup> This threshold was set at approximately the mode of the Sérsic *n* distribution for disk-dominated galaxies in Figure 7: below this value any Sérsic component can be safely considered representative of a disk.

↔ always considered a “disk”

Table 3 summarizes the scheme described above. Here the label “mixed” reflects the impossibility — due to the limitation imposed by the 2MASS data — to unambiguously decompose that Sérsic component into a bulge and a disk: this problem is addressed in §6.2. Out of the 335 *best-fit* models, we were able to directly decompose 274 ( $\sim 80\%$ ), while 62 ( $\sim 20\%$ ) contain a “mixed” component. For the decomposed galaxies, the bulge-to-total ratio (*B/T*) was defined as the ratio of the luminosities of the respective components, while for the “mixed” Sérsic objects it was defined using the concentration index, as explained in §6.2. Table 4 summarizes the statistics for the outcome of the 2D fitting procedure and for the results of the decomposition algorithms.

### 6.1 Estimation of uncertainty on bulge-to-total ratio (B/T)

To evaluate the uncertainty on a galaxy bulge-to-total ratio (*B/T*) we performed — for each object — a set of simulated fits in which the *B/T* was varied around the actual *best-fit* value. In practise, at each trial we arbitrarily re-distributed the galaxy total luminosity into a bulge and disk luminosities ( $L_{bulge}^{sim}$  and  $L_{disk}^{sim}$  respectively) in order to sample a simulated  $B/T^{sim}$  such that:

$$B/T^{sim} = L_{bulge}^{sim} / (L_{bulge}^{sim} + L_{disk}^{sim}). \quad (6)$$

The magnitudes of the *best-fit* bulge and disk components were fixed to the new values, and a new GALFIT fit was performed for each  $B/T^{sim}$ , for which we recorded the resulting  $\sigma_{XS}^{sim}$ , calculated as usual according to Equation 3. When  $\sigma_{XS}^{sim}$  is plotted against  $B/T^{sim}$ , it roughly traces a parabolic curve: representative examples of such plots are shown in Figure 6. The uncertainty on *B/T* was defined as the *B/T* at which the curve crosses the  $(\sigma_{XS} + \delta\sigma_{XS})$  limit, indicative of the upper statistical uncertainty on the fit. Although the uncertainties are not necessarily symmetrical, we assumed the average between the lower and the upper *B/T* values. We stress that the uncertainties obtained in this way do not strictly represent a Gaussian  $1-\sigma$  (or 68%) confidence level because the  $\Delta\sigma_{XS}$  has not been calibrated as an absolute statistic.

The disk and bulge luminosities were kept fixed throughout the fit; however, the other bulge and disk parameters (e.g., Sérsic *n*,  $R_e$ ) were let free to vary, in order not to excessively penalize the “artificial” *B/T* fits. Similarly, all the parameters of the other components of the SFRS target (e.g., the central AGN), as well as those of the other “contaminating” sources fit along, were frozen to prevent them from compensating for the less-than-optimal  $B/T^{sim}$ .

### 6.2 Further decomposition of “mixed” components

The “mixed” components are those Sérsic components to which our pipeline was unable to attribute a bulge or disk classification (see Table 3) because they represent an unknown mixture of the two. In order to infer the relative mass of the bulge (or equivalently, the bulge-to-disk ratio *B/D*) for the “mixed” components, one would be tempted to use the Sérsic index *n* as a summarizing parameter for the overall radial profile shape. However, several studies have highlighted that an improper Sérsic fit with a high index *n* can mimic e.g., a compact bulge superimposed on an extended disk. As a consequence, the Sérsic index is not a reliable indicator of the galaxy Hubble type (e.g., Graham & Worley 2008, their Figure 3). This issue is also present in our data.

DECISIONAL ALGORITHM FOR BULGE/DISK DECOMPOSITION				
MODEL	BULGE COMPONENT	DISK COMPONENT	MIXED COMPONENT	AGN COMPONENT
Sérsic <sup>n=1</sup>	–	Sérsic <sup>n=1</sup>	–	–
Sérsic <sup>n=4</sup>	Sérsic <sup>n=4</sup>	–	–	–
Sérsic	–	–	Sérsic $n > 1.5$	–
	–	Sérsic $n < 1.5$	–	–
Sérsic + psfAgn	–	Sérsic $n < 1.5$	–	psfAgn
	–	–	Sérsic $n > 1.5$	psfAgn
	psfAgn	Sérsic	–	–
Sérsic <sup>n=4</sup> + exDisk	Sérsic <sup>n=4</sup>	exDisk	–	–
Sérsic <sup>n=4</sup> + exDisk + psfAgn	Sérsic <sup>n=4</sup>	exDisk	–	psfAgn

**Table 3.** Components interpretation as bulge, disk, “mixed”, or AGN, according to each of the possible fit models.

FIT AND DECOMPOSITION SUMMARY	
SAMPLE GALAXIES	345
EXCLUDED GALAXIES	10
↪ All models failed	3
↪ All fits exceeded magnitude limit	7
GALAXIES WITH A BEST-FIT MODEL	335
↪ Decomposed	274
↪ Not decomposed	62

**Table 4.** Outcome of the fitting procedure and of the related bulge/disk decomposition algorithm. For the 62 galaxies we could not decompose via 2D fitting, we used the concentration of the surface brightness to infer the bulge-to-total ratio  $B/T$  (see §6.2).

To check whether the Sérsic index traces the bulge/disk decomposition obtained as described above, we considered two subsamples: the “candidate disk-dominated (DD) galaxies” and the “candidate bulge-dominated (BD) galaxies”. These are the galaxies in which the disk ( $L_{\text{disk}} > L_{\text{bulge}}$ ) or the bulge ( $L_{\text{bulge}} > L_{\text{disk}}$ ) component is dominant, respectively. Figure 7 presents the Sérsic index distribution from the single Sérsic fit to these two samples along with the corresponding distribution for the Sérsic fit to the whole sample. As expected, the vast majority of our targets are disk-dominated because the sample has been selected on the basis of star formation activity and hence biased towards late-type galaxies. There is a significant number of candidate DD galaxies which have been fit with an extremely large Sérsic index (up to  $n \sim 9$ ). This is indicative of the issue mentioned above, i.e., that in several cases an unphysically large  $n$  has erroneously compensated for an extended disk accompanied by a marginally resolved/bright bulge or a central AGN ( $\sim 80\%$  and  $\sim 20\%$  of the cases, respectively, for the DD galaxies with Sérsic index larger than 4). This precludes any chance to use our single-Sérsic-fit  $n$  to derive the missing  $B/D$ .

For galaxies with a “mixed” Sérsic component we resorted instead to the correlation between the concentration of the surface brightness and the  $B/T$ . In particular, we followed the method of e.g., [Gadotti \(2009\)](#) and [Lackner & Gunn \(2012\)](#), who used SDSS data to calibrate their  $B/T$  with respect to the concentration index  $C = R_{90}/R_{50}$  (see their Figure 5), where  $R_{90}$  and  $R_{50}$  are the radii enclosing 90% and 50% of the Petrosian flux, respectively

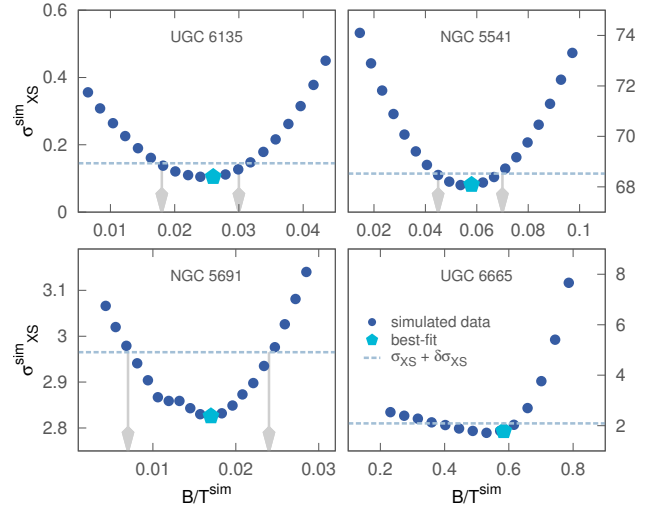


**Figure 6.** Examples of the technique used to estimate the uncertainty on  $B/T$ . Simulated GALFIT fits were performed by sampling values around the actual *best-fit*  $B/T$  and locking the luminosity of the bulge and disk components at the selected  $B/T^{\text{sim}}$ . The resulting  $\sigma_{XS}^{\text{sim}}$  measured at each iteration is recorded and then plotted against  $B/T^{\text{sim}}$  (blue points): the uncertainty on the *best-fit*  $B/T$  is estimated from the values (grey arrows) at which the curve hits the  $\sigma_{XS} + \delta\sigma_{XS}$  limit (dashed horizontal line). Notice that the *best-fit*  $\sigma_{XS}$  (light blue pentagon) does not necessarily fall exactly at the bottom of the curve (e.g., UGC 6665) because the fits are minimized on  $\chi^2$ , rather than on  $\sigma_{XS}$ .

([Petrosian 1976](#)). We calculated the concentration indices for the SFRS galaxies using the SDSS-DR12  $R_{90}$  and  $R_{50}$  derived in the  $z$ -band (the closest SDSS band to the 2MASS  $K_s$ -band) and calibrated them against the  $B/T$  for the targets for which we had a valid decomposition. A linear fit yielded:

$$B/T = 0.08 \times C(R_{90}/R_{50}) - 0.07 \quad (7)$$

with an RMS scatter of  $\sim 0.15$  around the best-fit line. In order to consider only unbiased concentration indices, we did not include in this analysis the sources hosting an AGN or those whose effective radius is comparable to the point-source FWHM (i.e., with  $R_e < 3.5''$ ). The calibration provided by Equation 7 was used to derive

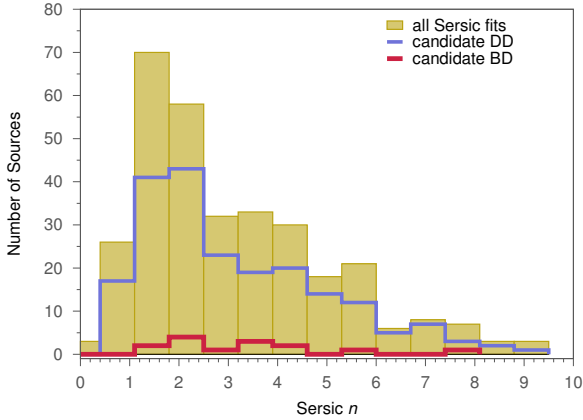


**Figure 7.** Sérsic index ( $n$ ) distribution for single Sérsic fit to the candidate disk-dominated (DD) galaxies (blue), candidate bulge-dominated (BD) galaxies (red), and for the Sérsic fit to all the objects (gold); bin size is  $\Delta n = 0.7$ . The candidate DD/BD galaxies are the objects in which the disk ( $L_{\text{disk}} > L_{\text{bulge}}$ ) or the bulge ( $L_{\text{bulge}} > L_{\text{disk}}$ ) luminosity is dominant, respectively (see §6.2). The distributions for the candidate DD and candidate BD galaxies do not sum up to the total sample because the galaxies we were not able to decompose do not appear in either of the sub-samples.

$B/T$  for the 62 galaxies lacking a direct GALFIT decomposition, and the relevant bulge and disk masses were calculated as the  $B/T$  fraction of the “mixed” component mass. The final decision on the model decomposition of each target is reported in Table D2.

### 6.3 Disk/bulge optical colors

For the 274 SFRS galaxies with a successful GALFIT decomposition, we retrieved the separate  $(u-r)$  colors for the disks and the bulges by performing 2D adaptive photometry on SDSS-DR12 images. Namely, we fit the  $u$  and  $r$ -band SDSS images by allowing the sub-components of each *best-fit* GALFIT model (derived in the 2MASS  $K_s$ -band; §5) to independently vary their magnitudes, while keeping all the other parameters (e.g., Sérsic  $n$ , axis ratio, P.A., etc.) constant, and resizing the radial scale lengths to match the SDSS pixel scale. Retaining consistent structural parameters comes at the cost of ignoring their wavelength dependence (e.g., Häußler et al. 2013)<sup>7</sup>, but this is justified because here we were only interested in retrieving integrated magnitudes, in which GALFIT has proven to excel (Häussler et al. 2007). For the SDSS fitting we produced object masks similar to those created for the 2MASS analysis (§4.1 and Appendix A3); in brief, we identified the sources in the SDSS images with SExtractor, and then masked all the contaminating objects except for the blended ones, which were fit simultaneously with the galaxies.

The left panel of Figure 8 shows the distributions of the bulge and disk  $u-r$  colours produced by our analysis. A Gaussian fit to the distributions yielded average colors  $(u-r)_b = 2.6$  mag and  $(u-r)_d = 2.0$  mag with standard deviations  $\sigma(u-r)_b = 1.0$  mag and  $\sigma(u-r)_d = 0.46$  mag for the bulges and disks respectively.

<sup>7</sup> Notice though that the work of Häußler et al. (2013) did not perform a full bulge/disk decomposition, but only adopted single Sérsic models, and therefore it is more sensitive to wavelength variations.

Figure 8 also shows colours from SDSS-DR12<sup>8</sup>: these magnitudes encompass the flux from whole galaxies and therefore represent the average colours of each galaxy’s bulge and disk. As SFRS is by construction a disk-dominated sample, it is not surprising that the global colour distribution is very close to that of the disks both in its peak ( $(u-r)_{\text{SFRS}} = 2.2$  mag) and width ( $\sigma(u-r)_{\text{SFRS}} = 0.43$  mag). The bulges present a wider colour distribution than disks, a reflection of the variety of secular and merger processes that lead to mass assembly in bulges. Nevertheless, the bulges’ average colours match those of red-sequence galaxies (Strateva et al. 2001, their Figure 2; Baldry et al. 2006, their Figure 7). The SFRS disks are on average  $\sim 0.5$  mag redder than typical blue-cloud galaxies. This difference is at least in part attributable to the sample selection: the SFRS includes star-forming galaxies sampled to cover almost uniformly 3 orders of magnitude in SFR, and it therefore includes objects living at the red edge of the blue cloud and in the green valley. The sample weighting will appropriately reduce the effects of these galaxies on luminosity and mass functions, but in unweighted numbers, they can bias the colors. Another effect might be that our bulge–disk separation was done at  $2.2 \mu\text{m}$  and might not be appropriate for determining  $u-b$  colors. Nonetheless, the maximum effect of an 0.5 mag colour error is a modest 11% in stellar mass difference (Equation B3).

The right panel of Figure 8 shows the bivariate  $(u-r)$  probability density of disks and bulges, calculated by means of a Gaussian kernel-density estimate. This plot provides the joint probability of a galaxy to host a disk *and* a bulge with a given color combination. The distribution exhibits a weak correlation, with redder disks being associated to redder bulges, indicating that star-forming galaxies evolve in parallel throughout their spatial extent. This is in line with our previous results showing that the local activity of a galaxy scales similarly to its global activity (Maragkoudakis et al. 2017a).

The disk/bulge colors derived in this section were used as stellar population proxies for the mass-to-light conversion of the disk/bulge  $K_s$ -band luminosities (Appendix B). For the galaxies which were not directly decomposed by our pipeline, but rather attributed a  $B/T$  through the procedure outlined in §6.2, we adopted the average color of the disk or bulge sub-population ( $\mu_{(u-r),d}$  or  $\mu_{(u-r),b}$ ) as the representative color of their disk or bulge fraction.

## 7 LUMINOSITY AND MASS FUNCTIONS

We built the luminosity function (LF) and stellar mass functions (MFs) adopting a variant of the  $1/V_{\text{MAX}}$  method (e.g., Rowan-Robinson 1968; Kafka 1967; Schmidt 1968), performed according to the following procedure.

- Count the number of sources per magnitude/mass bin.
- Correct for the selection effects (which we will refer to as “incompleteness”).
- Account for the Malmquist bias (i.e., the preferential detection of intrinsically bright objects). This is performed by dividing the counts in each bin by the surveyed volume  $V_{\text{MAX}}$ .

Steps *a* and *b* take into account that the SFRS sample has been defined based on the PSC $_z$  catalogue (Saunders et al. 2000), which is a  $60\mu\text{m}$  flux density limited catalogue. Therefore, we need to

<sup>8</sup> For the definition of the SDSS magnitudes refer to: [http://www.sdss.org/dr12/algorithms/magnitudes/#mag\\_model](http://www.sdss.org/dr12/algorithms/magnitudes/#mag_model).

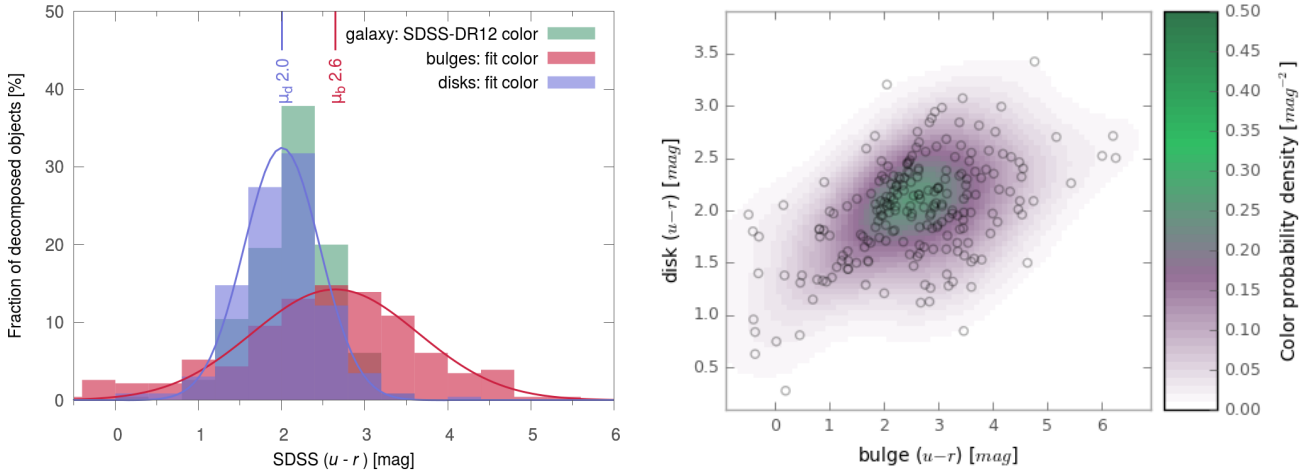


**Figure 8.** *Left* —  $(u-r)$  colour distribution of disks (blue histogram) and bulges (red histogram) yielded by our 2D fit of the SDSS-DR12 images for the 274 SFrs galaxies hosting both a disk and a bulge. The blue and red curves represent Gaussian fits to the distributions of disk and bulges, respectively; their means ( $\mu_d$  and  $\mu_b$ ) are indicated at the top of the figure. The green histogram shows the distribution of the global (“average”) galaxy color, directly obtained from the SDSS-DR12 catalogue. Note that all these magnitudes are expressed in the SDSS “maggy” native system, very close to the AB system. *Right* — The open circles present the measured bulge and disk colors for the 274 decomposed SFrs galaxies. The diffuse color gradient shows the bivariate  $(u-r)$  color density distribution, providing the probability of a given galaxy to host a disk *and* a bulge with a given color combination.

calculate the completeness for both the SFrs and the PSCz samples and the volume correction for the latter. The *actual* selection procedure that brought us from the PSCz down to the SFrs sample (Ashby et al. 2011) used a binning scheme that was not based solely on luminosity but involved also colors. Because we were interested in evaluating the completeness *only* as a function of luminosity, we had to derive a different selection function.

One potential bias related to the  $1/V_{MAX}$  method regards an overestimation of the LF at its faint end in case of non-homogeneous spatial distribution of sources (Willmer 1997; Takeuchi, Yoshikawa, & Ishii 2000; see also Johnston 2011 for an extended review), when compared to other methods such as e.g., the step-wise maximum likelihood (SWML; Efstathiou, Ellis, & Peterson 1988) or the  $C^-$  (Lynden-Bell 1971). However our analysis did not suffer from such bias, because the redshift distribution of our sample galaxies does not show any significant clustering, but it is rather a monotonically decreasing function of  $z$  (see Ashby et al. 2011). As described later in this section, the  $V_{MAX}$  was calculated on the 345 sample galaxies, and only *subsequently* corrected for selection effects, thus maintaining the spatial uniformity.

In §4 we prove the reliability of our method by applying the  $V/V_{MAX}$  test on the full PSCz sample. Similarly, the azimuthal distribution of the SFrs galaxies is not biased, since the sources are spread uniformly over the  $>20^\circ$  northern Galactic cap (see Ashby et al. 2011).

## 7.1 The PSCz sample

As mentioned in §2, the SFrs sample was selected from the PSCz catalogue (Saunders et al. 2000) of IRAS sources. Owing to the fact that the PSCz is itself complete down to its detection limits (0.6 Jy;

see Figure 1), it was used to assess the completeness of the SFrs sample. In order to calculate the selection function of SFrs with respect to its parent sample we first needed to obtain the distances of the PSCz objects in the same way as we did for the SFrs objects<sup>9</sup>, and apply the relevant K-correction (Oke & Sandage 1968).

The data for the full PSCz sample have been obtained through the *Vizier* service. The heliocentric velocities reported in the catalogue were corrected for the effects of local velocity fields (namely, the flows towards: Virgo, the Great Attractor, and the Shapley supercluster) using the recipe of Mould et al. (2000). These “cosmic velocities” were then used to recalculate the redshifts of the galaxy sample ( $z = v_{cosmic}/c$ ). For consistency, we applied the same correction to the SFrs sample: the velocities considered in this paper are therefore an updated version of the ones used in (Ashby et al. 2011).

We applied a K-correction to the PSCz 60  $\mu\text{m}$  flux assuming a power-law flux density spectrum  $f_\nu(\nu) \propto (\nu)^{-\alpha}$  and applying the prescription of Peterson (1997):

$$F_{int} = F_{obs} (1+z)^{\alpha-1} \quad (8)$$

where  $F_{int}$  is the intrinsic (true) flux emitted by the source within the rest-frame bandwidth, while  $F_{obs}$  is the received flux. We assumed a spectral slope  $\alpha \sim 2$ , thus simplifying Equation 8 to:

$$F_{int} = F_{obs} (1+z). \quad (9)$$

The chosen value for  $\alpha$  is appropriate for IR galaxies (e.g., Lawrence

<sup>9</sup> In this context, we applied to the PSCz catalogue the same coordinate and distance cuts that were originally applied to define the SFrs sample (see Ashby et al. 2011).



et al. 1986), and it has been previously adopted by Saunders et al. (1990) to construct the  $60\mu\text{m}$  luminosity function of PSCz galaxies (see Figure C1). At the median PSCz redshift ( $z \sim 0.02$ ), the K-correction yielded by Equation 9 is negligible (of the order of 2%).

The PSCz catalogue contains sources of different nature (including e.g., stars, H II regions, or planetary nebulae), out of which galaxies were selected by using the PSCz CLASS flag, which characterizes the object type<sup>10</sup>. We excluded 124 PSCz galaxies having  $v_{\text{cosmic}} < 500 \text{ km s}^{-1}$  (corresponding to  $d < 6.8 \text{ Mpc}$ , according to the Hubble law). Such low velocities are heavily affected by peculiar motions, and therefore the distances (and luminosities) of these galaxies cannot be calculated reliably from the Hubble law (e.g., Binney & Tremaine 1987). We accounted for this lost survey volume in our analysis (Section 7.3). After this screening we obtained the relevant SFRS parent sample, comprising 14 635 galaxies (as opposed to the 18 351 objects within the PSCz catalogue): in the remainder we will refer to this sample when mentioning the ‘‘PSCz’’.

## 7.2 Correction for sky coverage

The completeness of the SFRS sample is fully determined by the ‘‘weights’’ calculated in Ashby et al. (2011, see Table D2). These weights provide the ‘‘representativeness’’ of each SFRS source, i.e., how many galaxies it represents in the sky area of the PSCz survey, from which the SFRS sample is drawn. Specifically, the weights are calculated during the selection procedure, when the PSCz catalogue is split into 3D bins of SFR, sSFR and dust temperature, and a number of SFRS sources are selected out of each bin (see §2). The sum of all the SFRS weights therefore gives the total number of sources in the parent sample.

When constructing e.g., the  $K_s$ -band magnitude function, the completeness correction for a magnitude bin is simply the sum of all the weights of the SFRS galaxies falling within that bin. In practice, by doing this one marginalizes the SFRS galaxies’ weights along the variable of interest — in this example, the  $K_s$ -band magnitude. The same procedure was used in this work (in §7.6) to construct the completeness correction for the mass functions, this time by marginalizing over the mass variable.

To be precise, the actual completeness correction requires an additional factor due to the fact that the PSCz survey covers only 84% of the sky. Given that this spatial coverage was restricted by conditions independent from the  $K_s$ -band luminosity or the mass of the galaxies (nominally, it was limited by the IRAS coverage and spectroscopic follow-up; Saunders et al. 2000), the additional correction factor can be considered constant. Then, assuming a uniform distribution of the sources over the whole sky, the factor simply amounts to  $1 / 84\%$ .

The reliability of the completeness calculated following the procedure outlined above is discussed in Appendix C.

## 7.3 Calculation of $V_{MAX}$

The  $V_{MAX}$  represents the maximum volume up to which a source of luminosity  $L$  can be observed given the sample limiting flux  $F_{lim}$ . That is:

$$V_{MAX}(L) = \frac{4\pi}{3} \left( \frac{L}{4\pi F_{lim}} \right)^{3/2}. \quad (10)$$

<sup>10</sup> We considered bona-fide galaxies only the PSCz objects flagged as ‘‘go’’, ‘‘gf’’, or ‘‘gr’’

Because the SFRS sample is selected from the PSCz catalogue, we adopted — as  $F_{lim}$  — the IRAS  $60\mu\text{m}$  flux limit for PSCz:

$$F_{lim} = \nu_0 \cdot f_{60\mu\text{m}}^{lim} \cdot 10^{-23} = 3 \times 10^{-11} [\text{erg s}^{-1} \text{ cm}^{-2}], \quad (11)$$

where  $\nu_0$  is the central wavelength of the  $60\mu\text{m}$  filter ( $5 \times 10^{12} \text{ Hz}$ ),  $f_{60\mu\text{m}}^{lim}$  is the limiting flux density for the survey ( $\sim 0.6 \text{ Jy}$ ; Saunders et al. 2000), and the term  $10^{-23}$  is the conversion factor from Jy to  $\text{erg s}^{-1} \text{ cm}^{-2} \text{ Hz}^{-1}$ .

To construct the LF with the  $V_{MAX}$  method it is common to bin the data in luminosity, and for each bin calculate a  $V_{MAX}$  and adopt the central value of the bin as the luminosity defining the  $V_{MAX}$ . However, because the central value of a luminosity bin is not an accurate representation of a non-uniform distribution of the targets luminosities within the bin, nor does it take into account the different redshifts of the sources, we calculated the  $V_{MAX}$  on a source-by-source basis.

First, consider that the luminosity  $L$  appearing in Equation 10 is that of the fiducial source at luminosity distance  $d_{MAX}$  (corresponding to  $V_{MAX}$ ). As mentioned in §7.1, we calculated the true luminosities  $L_{corr}$  as they would be measured in the local frame of reference (by K-correcting for the actual distances of the sources). Imagine now to start ‘‘moving’’ the source away from the local frame of reference, up to  $d_{MAX}$ . The source’s true luminosity  $L_{corr}$  will decrease when observed back at the local frame of reference. To account for this, we introduced an ‘‘additional’’ K-correction. At any intermediate redshift  $z$  (between 0 and  $z_{MAX}$ ), the observed luminosity  $L_{obs}$  will be:

$$L_{obs}(z) = L_{corr}/K(z) \quad (12)$$

and the observed flux  $F_{obs}$  of a source at luminosity distance  $d$  will be:

$$F_{obs}(z) = \frac{L_{obs}(z)}{4\pi d^2} = \frac{L_{corr}/(1+z)}{4\pi d^2}, \quad (13)$$

where we assumed  $K(z) \sim (1+z)$  as in §7.1. Using the simple cosmology  $d = cz/H_0$ , Equation 13 can be expressed as:

$$F_{obs}(d) = \frac{L_{corr}/(1+d \cdot H_0/c)}{4\pi d^2}. \quad (14)$$

In order to find  $d_{MAX}$ , one should solve Equation 14 for  $d$  after setting  $F_{obs}(d) = F_{lim}$ . We solved this equation numerically. Figure 9 shows an example of the numerical evaluation of Equation 14 for a few sources of different  $L_{corr}$ , representative of the luminosity range of the SFRS sample (continuous lines). The maximum distance  $d_{MAX}$  at which a source of luminosity  $L_{corr}$  can be detected is that for which the observed flux  $F_{obs}$  curve (parametrized by Equation 14) hits the detection limit  $F_{lim}$  (black horizontal line). In this plot we also show the maximum distance that we would have calculated if we did not account for the additional K-correction ( $d_{MAX,classic}$ ). Notice that the discrepancy arising from the additional factor  $\frac{1}{(1+d \cdot H_0/c)}$  in Equation 14 increases for more distant objects. The slight bending of the  $F_{obs}$  curves kicks in when the additional K-correction becomes significant, and it is the cause of the aforementioned discrepancy between  $d_{MAX}$  and  $d_{MAX,classic}$  at high luminosities.

Similarly to Schmidt (1968), we evaluated the contribution of each SFRS target  $i$  to the source density within each bin in terms of the ‘‘density element’’  $\frac{1}{V_{MAX}}$ . The total source density  $\frac{dN}{dV}^{bin}$  within a magnitude bin is then:

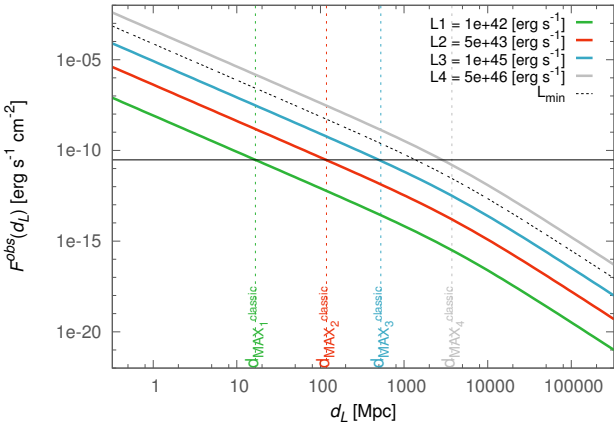


**Figure 9.** Graphical demonstration of the derivation of  $d_{MAX}$ . The continuous lines correspond to evaluations of Equation 14 as a function of the luminosity distance  $d_L$  for different values of source luminosity  $L_{corr}$  as shown in the legend. Each curve represents the observed flux  $F_{obs}$  of a source at different luminosity distances  $d_L$  after applying the relevant K-correction. The range of the plotted luminosities ( $L_{corr}$ ) is representative of the luminosity range of the SFRS sample. The dashed black line corresponds to the minimum luminosity  $L_{min}$  for which Equation 14 has real roots. The maximum distance  $d_{MAX}$  at which a source of luminosity  $L_{corr}$  can be detected is defined by when the corresponding  $F_{obs}$  curve hits the detection limit  $F_{lim}$  (black horizontal line). Dashed vertical lines show the  $d_{MAX}$  defined according to the “classical” definition (i.e., without accounting for the additional K-correction; dashed vertical lines).

$$\frac{dN^{bin}}{dV} = \sum_{i=1}^{N_{SFRS}^{bin}} \frac{w^i}{V_{MAX}^i(L_{60}^i)}, \quad (15)$$

where the summation is performed over all the sources contained in the bin, and  $w^i$  is the weight associated to the galaxy  $i$  (see §7.2). Note that we explicitly wrote  $V_{MAX}^i$  as  $V_{MAX}^i(L_{60}^i)$  because the volume element for source  $i$  is determined by the  $60\mu\text{m}$  luminosity of that source,  $L_{60}^i$ , as discussed earlier in this section. In practice, for each galaxy  $i$  in a given  $K$ -band bin we considered the corresponding  $60\mu\text{m}$  luminosity  $L_{60}^i$  and used it to calculate the relevant  $V_{MAX}^i(L_{60}^i)$ .

However, since the SFRS was drawn from the PSCz by selecting the  $60\mu\text{m}$  *brightest* objects in each bin of the three-dimensional sample selection scheme (see §2 and Ashby et al. 2011), the estimated volume is slightly biased with respect to the  $V_{MAX}$  we would have calculated if the SFRS had been randomly drawn from the PSCz sources in each bin. This discrepancy is illustrated in Figure 10, which shows (top panel) the distribution of the median  $V_{MAX}$  ( $\langle V_{MAX} \rangle$ ). The bottom panel shows the difference  $\delta\langle V_{MAX}^{bin} \rangle$ :

$$\delta\langle V_{MAX}^{bin} \rangle = \langle V_{MAX}^{bin} \rangle^{PSCz} - \langle V_{MAX}^{bin} \rangle^{SFRS}. \quad (16)$$

We correct for this bias by adding the appropriate  $\delta V_{MAX}^i$  to the  $V_{MAX}^i$  of each SFRS object. For this purpose we simply used the results shown in Figure 10, and for each galaxy  $i$  we picked the  $\delta\langle V_{MAX}^{bin} \rangle$  corresponding to the  $L_{60}$  bin in which the galaxy resides. Ultimately, the *effective*  $V_{MAX}$  for galaxy  $i$  ( $V_{MAX,eff}^i$ ) actually adopted in our analysis is:

$$V_{MAX,eff}^i = V_{MAX}^i(L_{60}^i) + \delta\langle V_{MAX}^{bin} \rangle|_{L_{60}^i \in bin} \quad (17)$$

Finally, from this volume we additionally subtracted a constant

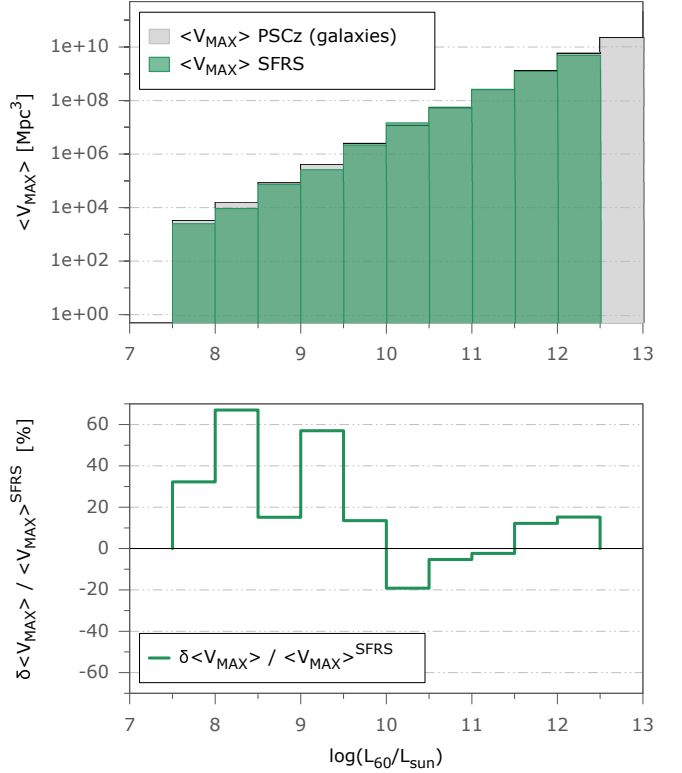


**Figure 10.** Distribution of  $V_{MAX}$  for the SFRS and for its parent PSCz sample. *Top* — Distribution of the median  $V_{MAX}$  calculated within each luminosity bin, for the SFRS (green) and the PSCz (grey) samples. *Bottom* — Relative difference ( $\delta\langle V_{MAX}^{bin} \rangle$ ; Equation 17) between the median  $V_{MAX}$  distributions shown above.

value corresponding to the minimum distance imposed during the selection of our sample ( $\sim 6.8$  Mpc; §7.1).

#### 7.4 $V/V_{MAX}$ test

The  $V/V_{MAX}$  test (Schmidt 1968) helps detect whether there are significant deviations from the uniform distribution of sources along the line of sight (as in the case of cluster of galaxies), which is a basic assumption in the definition of LF we are using. If we define  $V$  as the volume contained within the distance of a given source, then it is expected that, in a uniformly distributed sample, the average  $V/V_{MAX}$  is close to 0.5 (for a large number of sources). Figure 11 reports the results of the  $V/V_{MAX}$  test (where  $V_{MAX}$  was calculated according to the “classical” definition — Equation 10) for the whole PSCz sample. The uniform distribution of the data points shows that the PSCz sample is nearly unaffected by distribution biases.  $V/V_{MAX}$  slightly increases towards bright luminosities, shifting the average  $V/V_{MAX}$  slightly above 0.5. This effect is primarily due to the assumptions on the K-correction, which mostly affects the more distant (and hence brighter) objects. Nonetheless, this difference is very small ( $\sim 3\%$ ), and it does not significantly affect our analysis.

#### 7.5 SFRS $K_s$ -band luminosity function

Figure 12 shows the source density expressed in terms of  $h = H_0 / 100$ . The uncertainties were calculated by propagating the Poisson noise over the source counts in each bin. For small numbers

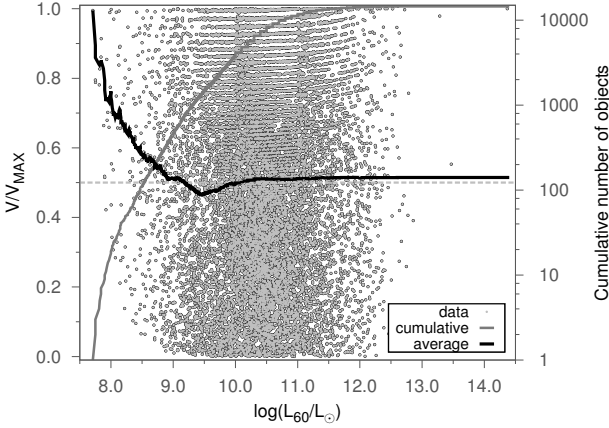


**Figure 11.**  $V/V_{MAX}$  test for the PSCz sample (grey dots). The black line shows the running average of the  $V/V_{MAX}$  ratio as a function of  $60\mu\text{m}$  luminosity. To show how many sources the running average is considering at a given luminosity, we also overplot a curve showing the cumulative number of objects (grey line, right ordinate). The running average reaches the  $V/V_{MAX} = 0.5$  value once  $\sim 1\%$  of the sample is included.

of counts ( $N < 5$ ), we calculated the uncertainties using the Gehrels (1986) approximation  $G_N$ :

$$G_N = 1 + \sqrt{0.75 + N} . \quad (18)$$

The top panel shows two fits to the LF; the first (blue solid line) is a fit to the Schechter function (Schechter 1976) in its magnitude form (Felten 1977):

$$\phi(M)dM = 0.4 \ln(10) \phi^* 10^{0.4(M^*-M)(\alpha+1)} \times \exp\left(-10^{0.4(M^*-M)}\right) dM . \quad (19)$$

This function behaves as a power law of index  $\alpha$  at low luminosities, and as an exponential at the high end. The value of  $M^*$  indicates the magnitude of transition between the two components, while  $\phi^*$  is a normalization factor. The second curve in the top panel (light blue dashed line) represents instead a fit to a double-Schechter function (e.g., Baldry, Glazebrook, & Driver 2008):

$$\begin{aligned} \phi(M)dM &= \phi_1(M)dM + \phi_2(M)dM \\ &= 0.4 \ln(10) \\ &\times \left( \phi_1^* 10^{0.4(M^*-M)\alpha_1} + \phi_2^* 10^{0.4(M^*-M)\alpha_2} \right) \\ &\times \exp\left(-10^{0.4(M^*-M)}\right) 10^{0.4(M^*-M)} dM . \end{aligned} \quad (20)$$

This function implements an outer exponential-like profile connected to a double inner power-law with logarithmic slopes  $\alpha_1$  and  $\alpha_2$ , such that  $\alpha_1 < \alpha_2$  (i.e.,  $\alpha_1$  regulates the behaviour at the faintest magnitudes). Here,  $\phi_1^*$  and  $\phi_2^*$  are the normalization factors of the separate Schechter components  $\phi_1(M)$  and  $\phi_2(M)$ , while  $M^*$  retains its meaning of transition point. The best-fit parameters for both the single- and double-Schechter fit are reported in Table 5. The two functions provide a similar fit to the data, and hence we will focus, for the rest of the paper, on the simpler (single-)Schechter function. Although consistent within the uncertainties, we observe an excess of brightest sources with respect to the Schechter fit in the last 2 magnitude bins. The most plausible explanation involves low-number statistics; in fact, before applying the completeness correction, these

bins contain only 1 source each. This feature is discussed further in §8.1.

Due to this discrepancy with the Schechter fit, we calculated the integrated luminosity density  $j$  from the direct summation of the  $1/V_{MAX}$  weighted luminosities of the SFRS sources rather than from the integration of the Schechter curve. Namely:

$$j = \sum_{i=1}^N \frac{w^i}{V_{MAX,eff}^i} \times 10^{-0.4(M_K^i - M_\odot)} , \quad (21)$$

where the first term in the summation represents the contribution to the LF from source  $i$ , which has  $K_s$ -band magnitude  $M_K^i$ . This yields  $j = 1.72 \pm 0.93 \times 10^9 L_\odot h^{-1} \text{Mpc}^{-3}$ .

## 7.6 SFRS stellar mass functions

The total stellar masses ( $M$ ) of the SFRS galaxies, as well as their disk and bulge sub-components (defined as summarized in Table 3), were calculated from their  $K_s$ -band luminosities by assuming a  $M/L$  ratio, as described in Appendix B. The stellar masses for the best-fit models are reported in Table D2. For the faint and/or noisy galaxies for which we could not obtain a fit to their 2D surface brightness, we used the total  $K_s$ -band luminosities from 2MASS (listed in Table D1), and we only report their total stellar mass (see §6).

We built the mass function MF, i.e., the number of sources per mass bin per  $\text{Mpc}^3$ , by simply summing the SFRS sources within each mass bin, after balancing by their weight and maximum volume, as calculated in the previous sections. Formally:

$$\phi(\Delta M_j) = \sum \frac{w^i}{V_{MAX,eff}^i} \quad (22)$$

$$\forall i \mid M_j - \Delta M_j < M_i < M_j + \Delta M_j ,$$

where  $\phi(\Delta M_j)$  is the mass function corresponding to the mass bin  $M_j \pm 0.5 \Delta M_j$ , the weight  $w^i$  is defined as discussed in §7.2, and  $V_{MAX,eff}^i$  is simply the  $V_{MAX,eff}^{bin}$  value for the  $60\mu\text{m}$  luminosity bin in which galaxy  $i$  resides (see Equations 15 and 17). Figure 13 and the top-left and top-right panels of Figure 14 show the total, disk and bulge mass functions, respectively. The uncertainties were calculated by propagating the Poisson noise of the source counts in each bin, as in the  $K_s$ -band luminosity function. In Appendix D we present the results of a Monte-Carlo simulation that we performed in order to verify that the Poissonian uncertainties we adopt are reliable. The top panel of Figure 13 shows a Schechter fit to the total MF of the form:

$$\phi(M)dM = \ln(10)(10^M) \frac{\phi^*}{M^*} \left(10 \frac{M}{M^*}\right)^\alpha \exp\left(-10 \frac{M}{M^*}\right) , \quad (23)$$

whose best-fit parameters are reported in Table 5.

Using the morphological information derived from the 2D surface brightness fit (§5), complemented by the concentration index decomposition (§6.2), we could measure the separate masses of the disk and bulge components of the sample galaxies. The  $M/L$  ratios for each component were calculated using the Bell et al. (2003) prescription (Appendix B; Equation B3). We calculated the stellar mass density for the whole sample ( $\rho_M$ ), and for the disks ( $\rho_{M,disks}$ ) and bulges ( $\rho_{M,bulges}$ ) sub-distributions, using the same formalism as in Equation 21, obtaining  $\rho_M = 4.61 \pm 2.40 \times 10^8 M_\odot h^{-1} \text{Mpc}^{-3}$ ,  $\rho_{M,disks} = 3.35 \pm 1.82 \times 10^8 M_\odot h^{-1} \text{Mpc}^{-3}$ , and  $\rho_{M,bulges} = 7.49 \pm 4.09 \times 10^7 M_\odot h^{-1} \text{Mpc}^{-3}$ .

A direct comparison between the disk and bulge mass functions is reproduced in the top panel of Figure 15. Notice that —

SCHECHTER FITS TO THE LF AND MF						
Model	$M_K^*$ [Mag - 5log( $h$ )]	$M^*$ [log( $h^2 M/M_\odot$ )]	$\alpha_1$	$\phi_1^*$ [ $dN h^3 \text{Mpc}^{-3} \text{dex}^{-1}$ ]	$\alpha_2$	$\phi_2^*$ [ $dN h^3 \text{Mpc}^{-3} \text{dex}^{-1}$ ]
(1)	(2)	(3)	(4)	(5)	(6)	(7)
LUMINOSITY FUNCTION						
Schechter	-22.84	-	-0.7	0.015	-	-
double-Schechter	-22.38	-	-0.8	0.017	1.2	0.006
MASS FUNCTION						
Schechter	-	10.41	-0.7	0.017	-	-

**Table 5.** Results of the single- and double-Schechter fits to the LF and MF.

(<sup>1</sup>) Model function. (<sup>2</sup>) Transition magnitude. (<sup>3</sup>) Transition mass. (<sup>4,6</sup>) Inner power law. (<sup>5,7</sup>) Normalization.

in this representation — the sum of the two curves does *not* yield the total mass function value in the corresponding bin because each galaxy is accounted for in both the disk and bulge mass functions (except for pure disks/bulges). In order to better visualize the contribution to the stellar mass budget per unit volume due to each stellar component, we define the “mass-density function”, i.e., the mass function multiplied by the central value of the mass bin:

$$\phi(M)M\Delta M = \int_{M-\Delta M}^{M+\Delta M} \phi(M)M\delta M. \quad (24)$$

The bottom panels of Figure 14 show the mass-density functions for disks and bulges, respectively, while in the bottom panel of Figure 15 the two are compared against the total mass-density function. In this representation, the *integral* mass densities of the disks and bulges *do* sum up to the total mass<sup>11</sup>.

As a final remark, we stress that the MFs presented in this work refer to *star-forming galaxies*, and to their bulges and disks. Passive galaxies will be an additional contribution to the MF. The underlying caveats of our work are the following.

- *Assumption on volume correction* — For the sub-component mass functions we adopted the volume correction calculated for the total MF (e.g., [Benson, Frenk, & Sharples 2002](#)). This implies that if a bulge/disk is present, then we detected it.
- *Caveat on completeness correction* — The SFRS objects are selected from the PSC<sub>z</sub> catalogue by binning it over the 3D parameter space defined by SFR, sSFR and dust temperature, and then selecting the brightest objects in each bin. The representativeness of a SFRS target is then given by its weight in that 3D bin (§7.2 and §7.3). Because the selection of the objects in each bin is based on flux, and not on luminosity (which could potentially be correlated with morphology), it does *not* bias the morphological demographics with respect to the parent sample. Therefore, the SFRS weights applied for the total MF also apply to the bulge and disk MFs.

## 8 DISCUSSION

### 8.1 Comparisons against other samples

Several factors can hamper the comparison between LFs (or MFs) derived in different studies. These include factors related to the

methodology (e.g., selection functions and completeness corrections, photometric systems, or even the analytical method used to build the LF/MF), or physical effects such as sample selection, redshift range, estimation of mass-to-light ratios, etc. With these limitations in mind, we present in this section a comparison of our functions against a selection of relevant studies addressing galaxies in the Local Universe. The cosmologies have been transformed to the one we assumed in §1 and the magnitudes converted to the Vega system. The bottom panel of Figure 12 (Figure 13) show the all the comparative LFs (MFs) discussed below.

*Luminosity Function* — First, we consider *K*-band LFs based on samples directly selected in the *K*-band. These are: the 2MASS galaxies of [Kochanek et al. \(2001\)](#), 4 192 galaxies, of which 2 192 are late-type objects) and [Devereux et al. \(2009\)](#), 1 613 bright galaxies), and the collection of 40 111 galaxies from the UKIRT Infrared Deep Sky Survey (UKIDSS) of [Smith, Loveday, & Cross \(2009\)](#). The first two studies have been chosen for a direct comparison against our 2MASS magnitudes, the last because it represents an extension of 2MASS towards fainter magnitudes ( $K \sim 18.3$  mag; [Hewett et al. 2006](#)). We additionally consider the LF derived by [Driver et al. \(2012\)](#) for the Galaxy And Mass Assembly (GAMA) sample: this refers to a slightly higher redshift than SFRS ( $0.013 < z < 0.1$ ) than that of SFRS ( $z \lesssim 0.05$ ), however it potentially encompasses all galaxy types in the nearby Universe and hence it offers a valuable reference for the overall galaxy population. Finally, we compare our LF against the one derived by [Xu et al. \(2006\)](#) for a sample of 161 galaxies selected in the far IR (FIR), similarly to SFRS<sup>12</sup>.

The most evident trend in 12 is the progressive disappearance of low-luminosity systems as source-selection wavelength increases. The SFRS sample was selected at 60  $\mu\text{m}$  to represent star-forming galaxies, and passive galaxies are therefore under-represented. Despite that, the SFRS agrees best with the *K*-band selected samples. In particular, our LF is a nearly exact match with the UKIDSS LF, and our LF exceeds the LF of the [Kochanek et al. \(2001\)](#) late-type subsample, as it should (despite the selection wavelength, the SFRS does include some early-type galaxies). Relative to the GAMA visible-light survey [Driver et al. \(2012\)](#), our sample shows a deficiency of dwarf systems, presumably passive dwarf ellipticals. However, in the range  $-24 \lesssim M_K \lesssim -19$  mag, our results agree with those of GAMA, implying that star-forming galaxies constitute nearly all the galaxies in that magnitude range. One possible caveat is that our sample is limited to a closer redshift range

<sup>11</sup> With the only caveat that the SFRS mass density for the 10 unsuccessful fits (see §5) was integrated using 2MASS data, while the same was not possible for the single disks or bulges

<sup>12</sup> For the sake of clarity, notice that [Xu et al. \(2006\)](#) present the separate LFs of a UV-selected and of a FIR-selected galaxy sample. In our comparison we are solely referring to the latter sample.



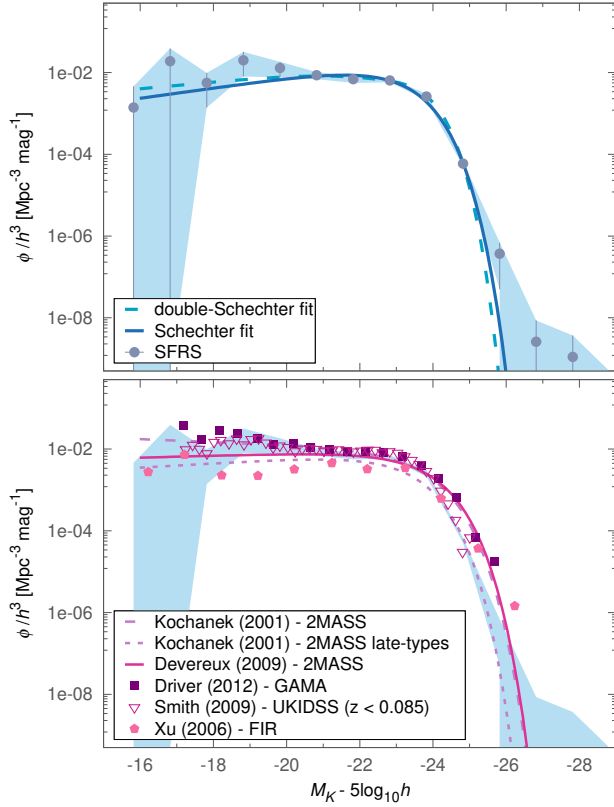


**Figure 12.**  $K_s$ -band luminosity function for the SFRS sample (blue dots), binned in  $\Delta M_K = 1.0$  mag bins. *Top* — Schechter (blue solid line) and double-Schechter (light blue dashed line) fit to the SFRS LF. *Bottom* — Same data as for the above panel, now compared with other studies. The curves refer to the 2MASS-based samples of Devereux et al. (2009, solid) and Kochanek et al. (2001, long-dashed: full sample, short-dashed: late-type sub-sample). The pentagons show the LF of FIR-selected galaxies of Xu et al. (2006), while the GAMA (Driver et al. 2013) and the UKIDSS (Smith, Loveday, & Cross 2009) LFs are represented by squares and triangles, respectively. Data points represent the actually measured LFs and the bands indicate their uncertainties, while the curves represent fits to Schechter functions extrapolated within our magnitude range.

LUMINOSITY FUNCTION			
$M_K$	$dN$	$\phi$	$\delta\phi$
[Mag - 5log( $h$ )]		[ $dN h^3 \text{ Mpc}^{-3} \text{ dex}^{-1}$ ]	[ $dN h^3 \text{ Mpc}^{-3} \text{ dex}^{-1}$ ]
(1)	(2)	(3)	(4)
-27.82	1	1.1e-09	2.6e-09
-26.82	1	2.6e-09	6.0e-09
-25.82	4	3.7e-07	3.2e-07
-24.82	42	5.9e-05	8.6e-06
-23.82	111	2.6e-03	4.6e-04
-22.82	87	6.4e-03	6.6e-04
-21.82	41	6.9e-03	1.3e-03
-20.82	35	8.6e-03	1.7e-03
-19.82	22	1.3e-02	5.3e-03
-18.82	12	2.0e-02	1.2e-02
-17.82	4	5.6e-03	4.2e-03
-16.82	4	1.9e-02	2.0e-02
-15.82	1	1.4e-03	3.2e-03

$j = 1.72 \pm 0.93 \times 10^9 [\text{L}_\odot h^{-1} \text{ Mpc}^{-3}]$

**Table 6.** Values for the SFRS LF (Figure 12) and luminosity density  $j$ .

(1) Bin central value ( $K$ -band absolute magnitude, Vega system); (2) Number of SFRS sources in the bin; (3) Source density; (4) Poisson uncertainty on source density.

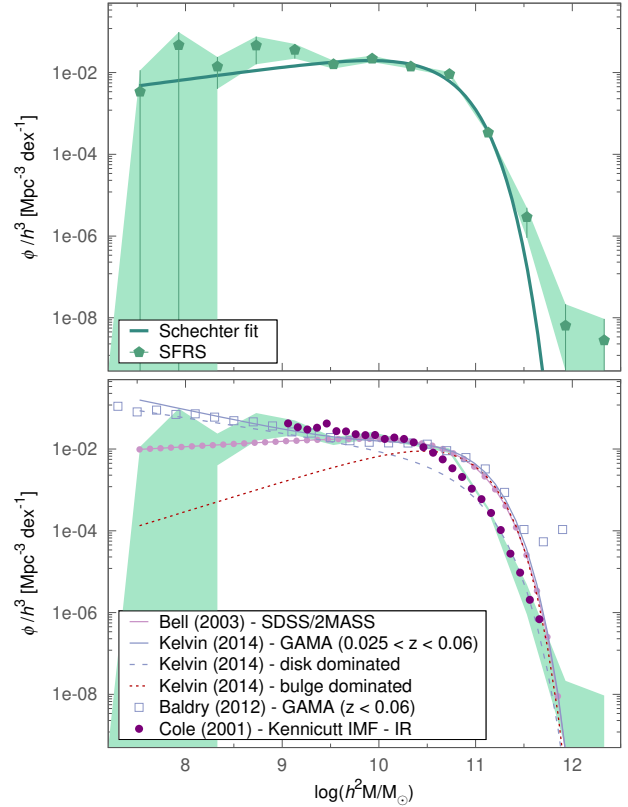


**Figure 13.** Stellar mass function for the SFRS sample (green data points), binned in 0.4 dex bins. *Top* — Schechter fit to the SFRS MF (green line). *Bottom* — As a comparison, we overplot the results from the studies of the mass functions of galaxies in the Local Universe by Bell et al. (2003, dotted pink curve), the GAMA MFs by Kelvin et al. (2014, dashed line) and Baldry, Glazebrook, & Driver (2008, empty squares), and the MF of IR-selected galaxies by Cole et al. (2001, violet data points). The MFs of Kelvin et al. (2014) is further subdivided into the MFs for their disk- and bulge-dominated systems. Data points represent the actually measured MFs and the bands indicate their uncertainties, while the curves represent fits to Schechter functions extrapolated within our mass range.

MASS FUNCTION: TOTAL			
$M$	$dN$	$\phi$	$\delta\phi$
[log( $h^2 M/M_\odot$ )]		[ $dN h^3 \text{ Mpc}^{-3} \text{ dex}^{-1}$ ]	[ $dN h^3 \text{ Mpc}^{-3} \text{ dex}^{-1}$ ]
(1)	(2)	(3)	(4)
7.53	1	3.4e-03	8.0e-03
7.93	4	4.7e-02	5.1e-02
8.33	4	1.4e-02	1.0e-02
8.73	11	4.6e-02	3.0e-02
9.13	23	3.6e-02	1.4e-02
9.53	28	1.6e-02	3.5e-03
9.93	41	2.2e-02	4.0e-03
10.33	74	1.4e-02	1.6e-03
10.73	111	9.2e-03	1.2e-03
11.13	58	3.4e-04	3.6e-05
11.53	7	2.9e-06	2.0e-06
11.93	1	6.4e-09	1.5e-08
12.33	1	2.8e-09	6.6e-09

$\rho_M = 4.61 \pm 2.40 \times 10^8 [\text{M}_\odot h^{-1} \text{ Mpc}^{-3}]$

**Table 7.** Values for the SFRS MF (Figure 13) and mass density  $\rho_M$ .

(1) Mass bin central value; (2) Number of SFRS sources in the bin; (3) Source density; (4) Poisson uncertainty on source density.

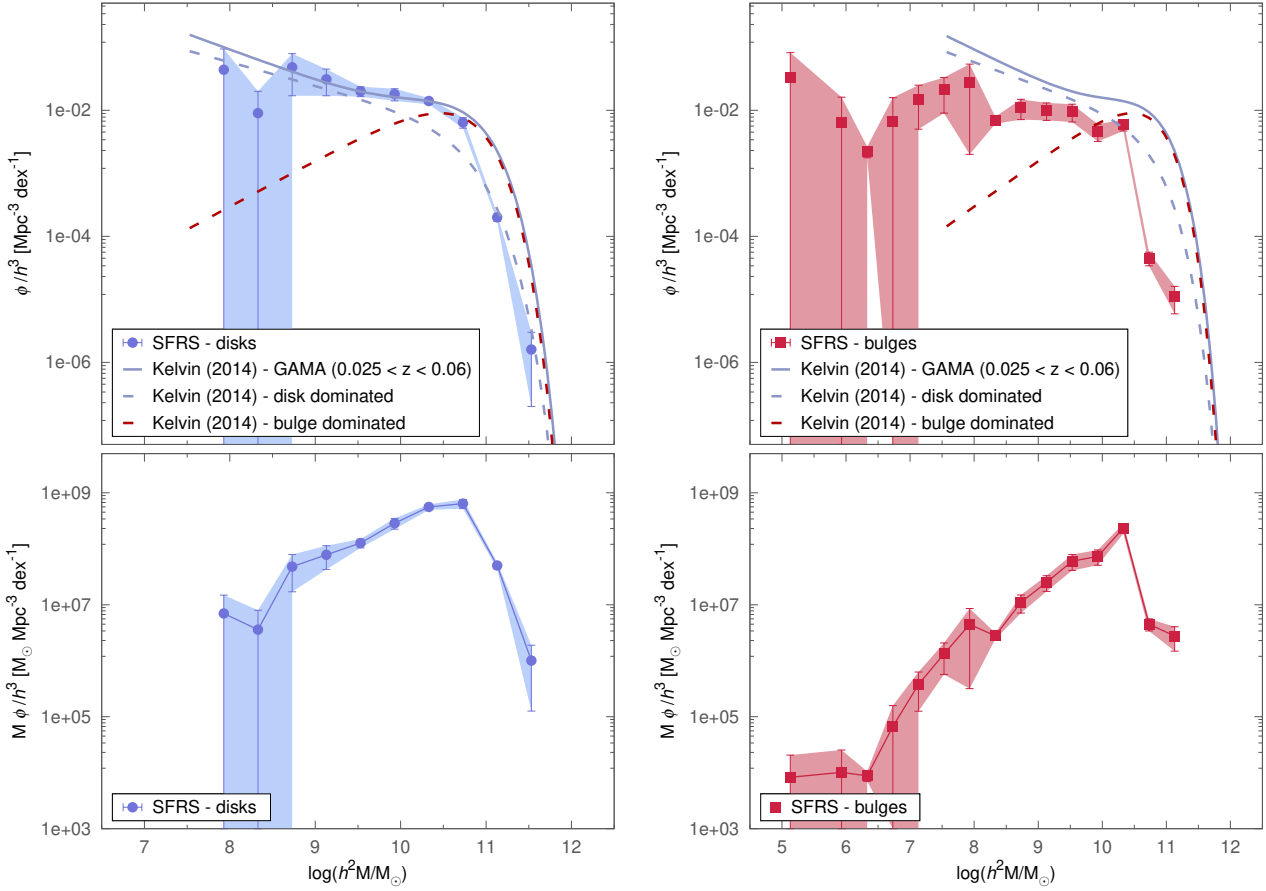


**Figure 14.** *Top* — Stellar mass function for the disk (*left*) and bulge (*right*) sub-components, binned in 0.4 dex bins, with shaded bands showing the 1- $\sigma$  uncertainties. As a comparison we overplot the mass function for the GAMA sample of nearby galaxies by Kelvin et al. (2014, solid curve), which is further subdivided into their MFs for the disk-dominated (blue dashed line) and bulge-dominated (red dashed line) objects. *Bottom* — Mass-density function for the disk (*left*) and bulge (*right*) sub-components defined by Equation 24.

MASS FUNCTION: DISKS			
M	$dN$	$\phi$	$\delta\phi$
$[\log(h^2 M/M_\odot)]$	$[dN h^3 \text{Mpc}^{-3} \text{dex}^{-1}]$	$[dN h^3 \text{Mpc}^{-3} \text{dex}^{-1}]$	$[dN h^3 \text{Mpc}^{-3} \text{dex}^{-1}]$
(1)	(2)	(3)	(4)
7.93	4	4.4e-02	5.0e-02
8.33	2	9.0e-03	1.1e-02
8.73	10	4.8e-02	3.1e-02
9.13	21	3.1e-02	1.4e-02
9.53	32	2.0e-02	3.6e-03
9.93	40	1.8e-02	3.9e-03
10.33	81	1.4e-02	1.6e-03
10.73	97	6.4e-03	1.2e-03
11.13	35	2.0e-04	2.7e-05
11.53	4	1.6e-06	1.4e-06

$$\rho_{M,disks} = 3.35 \pm 1.82 \times 10^8 [M_\odot h^{-1} \text{Mpc}^{-3}]$$

**Table 8.** Values for the disk MF (Figure 14) and mass density  $\rho_{M,disks}$ .

(1) Mass bin central value; (2) Number of SFRS sources in the bin; (3) Source density; (4) Poisson uncertainty on source density.

MASS FUNCTION: BULGES			
M	$dN$	$\phi$	$\delta\phi$
$[\log(h^2 M/M_\odot)]$	$[dN h^3 \text{Mpc}^{-3} \text{dex}^{-1}]$	$[dN h^3 \text{Mpc}^{-3} \text{dex}^{-1}]$	$[dN h^3 \text{Mpc}^{-3} \text{dex}^{-1}]$
(1)	(2)	(3)	(4)
5.13	1	3.3e-02	4.9e-02
5.93	1	6.4e-03	9.7e-03
6.33	2	2.2e-03	4.4e-04
6.73	2	6.7e-03	9.1e-03
7.13	9	1.5e-02	1.0e-02
7.53	10	2.1e-02	1.2e-02
7.93	15	2.8e-02	2.6e-02
8.33	14	7.0e-03	9.0e-04
8.73	19	1.1e-02	3.9e-03
9.13	31	1.0e-02	3.1e-03
9.53	59	9.5e-03	3.0e-03
9.93	69	4.6e-03	1.4e-03
10.33	50	5.9e-03	1.2e-03
10.73	12	4.5e-05	1.1e-05
11.13	6	1.1e-05	5.1e-06

$$\rho_{M,bulges} = 7.49 \pm 4.09 \times 10^7 [M_\odot h^{-1} \text{Mpc}^{-3}]$$

**Table 9.** Values for the bulge MF (Figure 14) and mass density  $\rho_{M,bulges}$ .

(1) Mass bin central value; (2) Number of SFRS sources in the bin; (3) Source density; (4) Poisson uncertainty on source density.

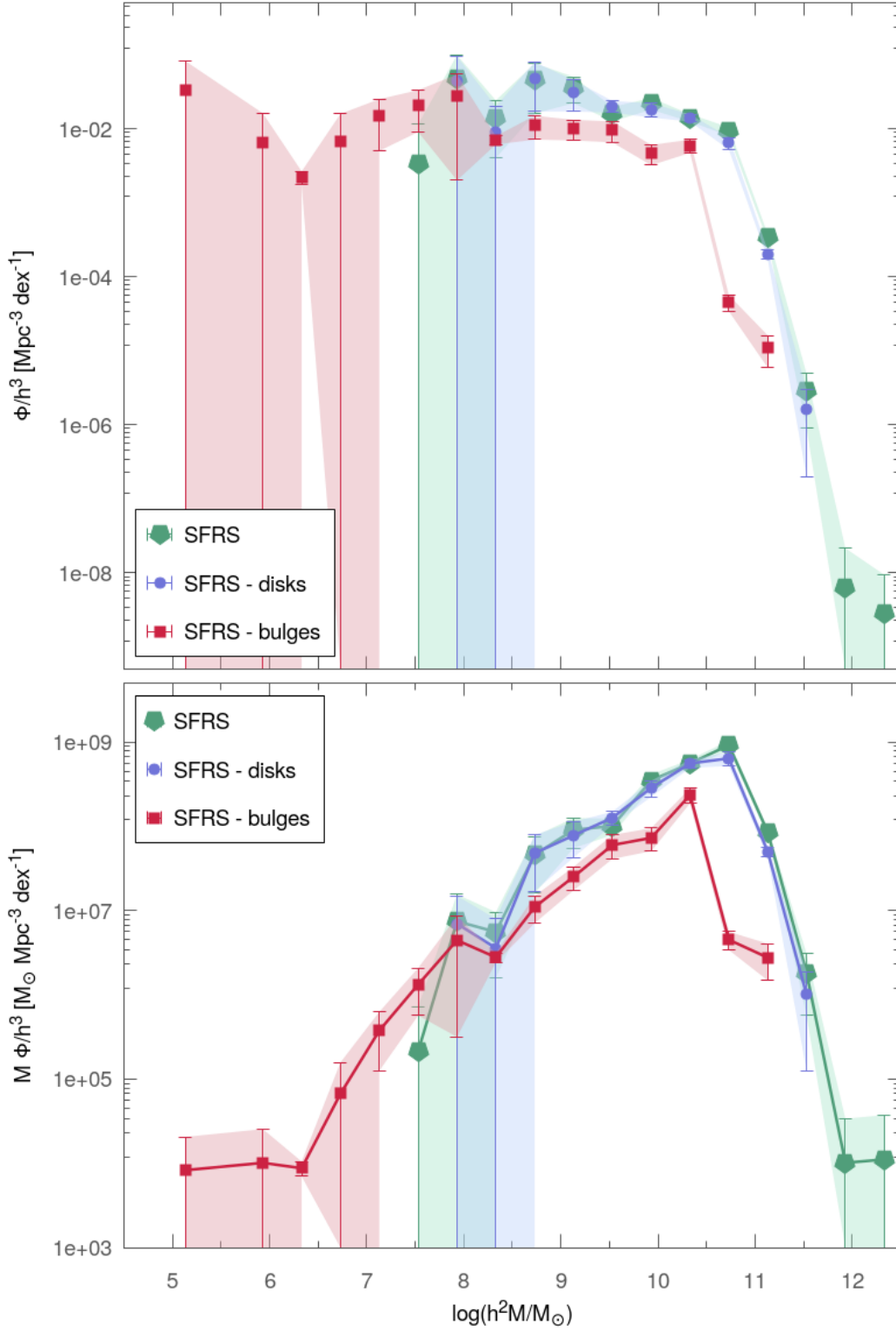


**Figure 15.** Comparison of total (green diamonds), disk (blue dots), and bulge (red squares) mass (*top*; Equation 23) and mass-density (*bottom*; Equation 24) functions, binned in 0.4 dex bins. The 1- $\sigma$  confidence range shown by the shaded regions were calculated by propagating the Poisson uncertainty over the source counts in each bin.

than GAMA or UKIDSS, and local density enhancements can yield overestimates up to a factor of two (e.g. Karachentsev et al. 2004). In comparison to the SFRS and all the other surveys, the FIR LF of Xu et al. (2006) gives systematically smaller density counts for luminosities smaller than  $L^*$  ( $M_K \gtrsim -23$ ). However, it shall be noted that their data have large uncertainties due to the low-number statistics (see their Figure 7) which can partially reconcile their LF with ours. If the bias was real, it could be attributed to the significantly different morphological census: that of Xu et al. (2006) is composed of  $\sim 39\%$  interacting systems or peculiar galaxies, while SFRS contains a much lower fraction of such objects. We can rule out an inaccurate completeness correction as the source of the difference, because both our study (see Figure C1) and that of Xu et al. (2006) correctly reproduce the  $60\mu\text{m}$  LF of the parent sample<sup>13</sup>. We argue instead that the difference arises from the construction of the LF: Xu et al. (2006) built their  $K$ -band LF using the conditional probability to find a FIR-selected galaxy of a given  $K$  magnitude within the combined UV +  $60\mu\text{m}$  luminosity bin (see their Section 3.3 and their Equation 1 and 2), while we directly calculate the  $K$ -band number counts. Alternatively, we also consider that SFRS may be biased against metal-poor dwarf galaxies, which present low IR emission but strong UV luminosities.

*Mass Function* — As a first comparison we consider the mass function by Cole et al. (2001), which is based on a NIR-selected sample (2MASS). Secondly, we consider the work by Bell et al. (2003), whose prescriptions we used to estimate the  $M/L$  ratios and ultimately the SFRS stellar masses (Equation B3). Their study regards a magnitude-limited, optically-selected sample of SDSS galaxies with available 2MASS counterparts. Finally — as for the LF — we selected the GAMA survey as a benchmark to evaluate the selection bias in our IR-selected sample with respect to the general galaxy population. Baldry et al. (2012) presented a GAMA MF restricted to a redshift range ( $z < 0.06$ ) very close to that of SFRS ( $z \lesssim 0.05$ ). Kelvin et al. (2014) studied the GAMA MF on a slightly narrower redshift range ( $0.025 < z < 0.06$ ), but offered a decomposition of their MF into disk- and bulge-dominated systems.

Our total mass function exactly traces the data points of Cole et al. (2001) throughout the extent of their mass sampling. Our MF is also largely consistent with the curve of Bell et al. (2003) at the low mass range ( $\log(h^2 M/M_\odot) \sim 7.5\text{--}10.5$ ). Similarly to the LF, the low-end “upturn” displayed by the GAMA mass functions is not observed in the SFRS MF. Additionally, the comparison against both the GAMA and the Bell et al. (2003) curves highlights a lack of objects at masses larger than  $M^*$  (this feature is less evident in the LF). These are likely to be passive galaxies, which are missing from the SFRS.

*Lack of upturn at the low-end* — As mentioned above, one of the most noticeable features of both our LF and MF is that they fall below (but consistent within the uncertainties) the studies based on visible-light selection (Baldry, Glazebrook, & Driver 2008). Most probably this happens because low luminosity/mass galaxies lack the necessary dust amount to efficiently reprocess the radiation from young stellar populations into IR emission (e.g., Dale et al. 2009; Calzetti et al. 2010). In fact, dwarf galaxies tend to have lower metallicities and hence higher gas-to-dust ratios than more massive systems. It follows that these objects are under-represented in our sample, which is primarily selected based on  $60\mu\text{m}$  luminosity (§2).

<sup>13</sup> The completeness for the Xu et al. (2006) sample has been studied by Iglesias-Páramo et al. (2006).

Interestingly, the upturn is undetected in  $K$ -band studies as well (see the UKIDSS LF or the Bell et al. 2003 MF). Baldry, Glazebrook, & Driver (2008) argued that those surveys do not properly probe down to their declared surface brightness limit: a similar issue might in principle affect our data. However, Driver et al. (2012) argued that the upturn in their GAMA LF is due to the combination of the LF of elliptical galaxies — forming a plateau below  $M^*$  — plus the tail of LF of the star-forming sub-population (see their Figure 13). This is consistent with the lack of upturn in our functions, because in the SFRS sample ETGs are rare by construction.

*Behaviour at the high-end* — The SFRS MF, and to a lesser degree the SFRS LF, display a clear deficiency of high mass/luminosity objects with respect to the general galaxy population of GAMA. The morphologically-separated curves by Kelvin et al. (2014) show that the lack of objects above  $M^*$  is likely the result of the different sample selection: the SFRS consists of star-forming galaxies, and therefore it is biased against passive bulge-dominated objects which populate the high-mass end. In the last 1–2 data points corresponding to the most luminous (massive) LF (MF) bins, our data show a deficiency with respect to the general trend, although such difference is not significant given the large uncertainties.

Driver et al. (2012) observed a similar feature in their data and argued that this is related to a sub-population of high-Sérsic index ETGs. The average Sérsic index we obtained by the single Sérsic fit (§4.1) to the 10 most luminous SFRS galaxies is only  $\sim 4.5$ , far from being in the highest Sérsic index tier of our sample (see Figure 7). Moreover, as shown by Figure 15, disks can significantly contribute to the high-end of the SFRS MF, hence we exclude any involvement of high-Sérsic index ETGs in our case.

*Morphological type and colour* — Remarkably, the LF of late-type galaxies of Kochanek et al. (2001, Figure 12) does not completely follow the SFRS LF throughout the entire magnitude range: there is agreement only at the low-end. Similarly, neither the bulge- nor the disk-dominated curve of Kelvin et al. (2014, Figure 13) agrees with the SFRS MF over the entire mass range. This shall not be surprising since star-forming galaxies are not expected to be exclusively disk-dominated (or bulge-dominated, for what matters). Instead, they contain a varying mixture of both bulge and disk components. In other words, star-forming galaxies cannot be sharply identified by their morphological appearance; on the contrary, they populate all mass ranges and all Hubble types. This is consistent with the trends in the Kelvin et al. (2014) MFs, where the bulge-dominated MF agrees well with the high-end of the SFRS MF, while the disk-dominated MF of Kelvin et al. (2014) agrees with the low-mass end of our MF.

## 8.2 Mass repartition in bulges and disks

The discussion in §8.1 lead to the conclusion that an arbitrary morphological separation into late- and early-types or disk- and bulge-dominated galaxies does not uniquely characterize the population of star-forming galaxies: star formation takes place in a wide range of galaxies’ morphological components (e.g., Kennicutt 1998).

In this context, it is more meaningful to study the distribution of mass into disks and bulges. Our mass-density functions (bottom panel of Figure 15) show that for the range  $10^8\text{--}10^{10} M_\odot$  the contribution of disks and bulges to the mass density in the Local Universe is closely comparable. Moreover, both distributions have their maximum close to the global MF maximum ( $M^*$ ; i.e.,  $\log(h^2 M/M_\odot) \sim 10.41$ , see Table 5), where they also display similar peak values (within a factor of  $\sim 3$  of each other). By broadly



associating bulge mass with an old stellar population and disk mass with recently formed stars, the similarity of the peak locations and amplitudes implies that the *average* star-forming galaxy assembled as much mass in the distant past as it did in its latest evolution. The galaxy mass functions are a key metric for testing and calibrating cosmological galaxy evolution models (e.g., Crain et al. 2015). The evolution of galaxy morphology (e.g. fraction of disk and bulge dominated galaxies) is another such metric (e.g., Parry, Eke, & Frenk 2009). The presented bulge and disk mass functions provide yet another metric for testing and calibrating galaxy evolution simulations.

A more detailed inspection of the mass-density functions reveals that bulges alone populate the bottom range of the distribution ( $\log(h^2 M/M_\odot) \lesssim 7.5$ ), while disks largely monopolize the high-mass end, indicating that star-forming galaxies host most of their mass in their disks. Adopting the previous assumption that disk (bulge) mass is associated with recent (past) stellar formation, the ratio of the disk to bulge density functions can serve as a proxy of the “timescale” of star formation as a function of mass. For example, following on the consideration that in massive objects the disk density largely dominates, the high-mass end is where most recent star formation happened. Starting from their morphologically decomposed MFs and assuming an average  $B/T$ , Kelvin et al. (2014) estimated that 50% of the stellar mass in the Local Universe resides in bulge structures. With our bulge/disk decomposition we show that this conclusion does not hold, at least for star-forming galaxies. Instead, our integrated stellar densities (Tables 8 and 9) indicate a ratio 4:1 in favour of disks.

The fact that star formation activity happens where most of the mass is concentrated (i.e., in disks) further confirms that mass is the primary parameter characterizing galaxy evolution. This is in agreement with the galaxy main sequence (e.g., Elbaz et al. 2011) as well as with the sub-galactic main sequence (e.g., Maragkoudakis et al. 2017a), where we find that more massive systems (either galaxies or individual star-forming regions) also host higher SFR. To further explore this, in a forthcoming SFRS paper we will additionally present the specific SFR (sSFR) and the bivariate (mass vs. sSFR) volume-weighted functions, the latter being the most accurate representation of the star-forming main sequence.

## 9 SUMMARY AND CONCLUSIONS

We obtained archival  $K_s$ -band 2MASS data (§3) for the galaxies composing the sample of the Star Formation Reference Survey (SFRS), with the ultimate intent of studying the stellar mass function in star-forming galaxies, and the distribution of stellar mass in their disk and bulge sub-components.

We designed a sophisticated bulge/disk decomposition routine based on the software GALFIT for the 2D fit of the surface brightness of galaxies (§4). The *best-fit* model was automatically selected primarily based on the “excess variance” (Vaughan et al. 2003), providing a better statistic than the commonly adopted  $F$ -test. The parametric components of the selected model were attributed a physical meaning (i.e., bulge, disk, or AGN) through a decisional tree which accounts for unresolved bulges (§6). The galaxy luminosities were converted to stellar masses using the Bell et al. (2003) prescriptions and using archival SDSS-DR12 ( $u-r$ ) colors as proxies for the global stellar population. For the disk/bulge sub-components we instead determined the separate colors by applying our decomposition to the SDSS  $u$  and  $r$  images (§6.3), producing the bivariate color distribution, which provides the joint probability of a galaxy

to host a disk *and* a bulge with a given color combination (Figure 8). We built the SFRS luminosity function (Figure 12) using the  $1/V_{MAX}$  method, after correcting the source density by selection biases (§7.2), and correcting the volume by the effects of lost survey area (§7.3). Similarly, we produced the mass function for the SFRS galaxies (Figure 13) and for their disk- and bulge- sub-components (Figure 14), which we also represented in terms of mass-density function (Figures 14 and 15) to highlight contribution of each component to the total mass density.

Our main conclusions can be summarised as follows.

- The SFRS  $K_s$ -band LF and MF agree with previous studies based on similarly selected samples. In particular, the LF resembles that of  $K$ -band selected samples and is broadly compatible with that of FIR-selected studies. Likewise, the SFRS MF traces remarkably well that of 2MASS- and IR-selected samples (§8.1).
- The star-forming galaxy number density is lower than that of the general galaxy population — as probed by the GAMA and  $K$ -band surveys — at both ends of the LF and MF. We interpret these features in terms of the different sample selection (§8.1). At the faint/low-mass end, dwarf galaxies are under-represented in the SFRS due to the lack of dust content able to produce significant emission in the  $60\mu\text{m}$  luminosity band, which is the primary selection band for the SFRS sample. At the bright/high-mass end, “dead” early-type systems do not contribute to the population of star-forming galaxies, and hence the LF (MF) is intrinsically lower.
- Star-forming galaxies cannot be identified with specific galaxy sub-samples identified via a morphological separation (e.g., late-type or disk-dominated systems) or via their color (§8.1).
- Despite the *mean* star-forming galaxy roughly equally sharing its stellar mass between its disk and bulge components, most of the mass of currently star-forming objects is stored in their disks rather than bulges (4:1; §8.2). This information, combined with the fact that disks dominate the high-mass end of the MF, has two implications: 1) that most recent star formation happened in massive systems, and 2) that mass is the primary parameter in the study of star forming objects.

The last result confirms the general scenario depicted by the main sequence of star-forming galaxies (e.g., Elbaz et al. 2011). However, our mass-density functions now constitute an accurate benchmark for models addressing the mass assembly in bulges/disks in that they quantify for the first time the relative density of stellar mass stored in the sub-components of star-forming objects (which — as our MF shows — compose the vast majority of local galaxies). This can in turn be used to investigate the evolution of star formation activity.

## ACKNOWLEDGMENTS

We wish to thank T. Bitsakis, and J. Fritz for the useful assistance along the development of the analysis techniques. PB and AZ acknowledge support by the EU IRG grant 224878. Space Astrophysics at the University of Crete was supported by EU FP7-REGPOT grant 206469 (ASTROSPACE). This project has received funding from the European Union’s Horizon 2020 research and innovation programme under the Marie Skłodowska-Curie RISE action, grant agreement No 691164 (ASTROSTAT). The research leading to these results has received funding from the European

Research Council under the European Union's Seventh Framework Programme (FP/2007-2013) / ERC Grant Agreement n. 617001. This publication makes use of data products from the Two Micron All Sky Survey, which is a joint project of the University of Massachusetts and the Infrared Processing and Analysis Center/California Institute of Technology, funded by the National Aeronautics and Space Administration and the National Science Foundation. This research has made use of the VizieR catalogue access tool, CDS, Strasbourg, France.

## DATA AVAILABILITY

The data underlying this article are available in the article and in its online supplementary material. The photometric measurements from the 2MASS-PSC and -XSC catalogues were derived via VizieR: <https://vizier.u-strasbg.fr/viz-bin/VizieR>. The 2MASS datasets were derived from sources in the public domain: <https://irsa.ipac.caltech.edu/applications/2MASS/IM>. The SDSS datasets were derived from sources in the public domain: <http://skyserver.sdss.org/dr12/en/home.aspx>.

## REFERENCES

- Andreon S., 2002, *A&A*, 382, 495
- Ashby M. L. N., et al., 2011, *PASP*, 123, 1011
- Baldry I. K., Balogh M. L., Bower R. G., Glazebrook K., Nichol R. C., Bamford S. P., Budavari T., 2012, *MNRAS*, 421, 621
- Baldry I. K., Glazebrook K., Driver S. P., 2008, , 388, 945
- Baldry I. K., et al., 2012, *MNRAS*, 421, 621
- Beichman C. A., Chester T. J., Skrutskie M., Low F. J., Gillett F., 1998, *PASP*, 110, 480
- Bell E. F., McIntosh D. H., Katz N., Weinberg M. D., 2003, *ApJS*, 149, 289
- Benson A. J., Frenk C. S., Sharples R. M., 2002, *ApJ*, 574, 104
- Bertin E., Arnouts S., 1996, *A&AS*, 117, 393
- Bertin E., Mellier Y., Radovich M., Missonnier G., Didelon P., Morin B., 2002, *ASPC*, 281, 228
- Bertin E., 2011, *ASPC*, 442, 435
- Bevington P. R., Robinson D. K., 2003, *Data reduction and error analysis for the physical sciences*, 3rd ed., McGraw-Hill, Boston, MA
- Binney J., Tremaine S., 1987, , *Galactic Dynamics*, Princeton University Press, Princeton, NJ
- Bonfini P., Dullo B. T., Graham A. W., 2015, *ApJ*, 807, 136
- Brown T., et al., 2017, *MNRAS*, 466, 1275
- Bruzual G., Charlot S., 2003, *MNRAS*, 344, 1000
- Calzetti D., et al., 2010, *ApJ*, 714, 1256
- Chilingarian I. V., Melchior A.-L., Zolotukhin I. Y., 2010, *MNRAS*, 405, 1409
- Ciambur B. C., 2016, *PASA*, 33, e062
- Cole S., et al., 2001, *MNRAS*, 326, 255
- Crain R. A., Schaye J., Bower R. G., Furlong M., Schaller M., Theuns T., Dalla Vecchia C., et al., 2015, *MNRAS*, 450, 1937
- Cutri R. M., et al., 2003, *yCat*, 2246
- Dale D. A., et al., 2009, *ApJ*, 703, 517
- Damjanov I., et al., 2009, *ApJ*, 695, 101
- Devereux N. A., Becklin E. E., Scoville N., 1987, *ApJ*, 312, 529
- Devereux N., Willner S. P., Ashby M. L. N., Willmer C. N. A., Hriljac P., 2009, *ApJ*, 702, 955
- Driver S. P., et al., 2012, *MNRAS*, 427, 3244
- Driver S. P., Robotham A. S. G., Bland-Hawthorn J., Brown M., Hopkins A., Liske J., Phillipps S., Wilkins S., 2013, *MNRAS*, 430, 262 2
- Efstathiou G., Ellis R. S., Peterson B. A., 1988, *MNRAS*, 232, 431
- Elbaz D., et al., 2011, *A&A*, 533, A119
- Felten J. E., 1977, *AJ*, 82, 861
- Gadotti D. A., 2009, *MNRAS*, 393, 1531
- Gehrels N., 1986, *ApJ*, 303, 336
- Graham A., Lauer T. R., Colless M., Postman M., 1996, *ApJ*, 465, 534
- Graham A. W., Worley C. C., 2008, *MNRAS*, 388, 1708
- Häußler B., et al., 2013, *MNRAS*, 430, 330
- Häussler B., et al., 2007, *ApJS*, 172, 615
- Hewett P. C., Warren S. J., Leggett S. K., Hodgkin S. T., 2006, *MNRAS*, 367, 454
- Ho L. C., Filippenko A. V., Sargent W. L. W., 1993, *ApJ*, 417, 63
- Holwerda B. W., 2005, *Source Extractor for Dummies v5* (arXiv:astro-ph/0512139)
- Hopkins P. F., Hernquist L., Cox T. J., Di Matteo T., Robertson B., Springel V., 2006, *ApJS*, 163, 1
- Hopkins P. F., et al., 2010, *ApJ*, 715, 202
- Iglesias-Páramo J., et al., 2006, *ApJS*, 164, 38
- Jedrzejewski, R. I. 1987, *MNRAS*, 226, 747
- Jarrett T. H., Chester T., Cutri R., Schneider S., Skrutskie M., Huchra J. P., 2000, *AJ*, 119, 2498
- Johnston R., 2011, *A&ARv*, 19, 41
- Kafka P., 1967, *Natur*, 213, 346
- Karachentsev I. D., Karachentseva V. E., Huchtmeier W. K., Makarov D. I., 2004, *AJ*, 127, 2031
- Kelvin L. S., et al., 2014, *MNRAS*, 444, 1647
- Kennicutt R. C., Jr., 1998, *ARA&A*, 36, 189
- Kirby E. M., Jerjen H., Ryder S. D., Driver S. P., 2008, *AJ*, 136, 1866
- Kochanek C. S., et al., 2001, *ApJ*, 560, 566
- Kouroumpatzakis K., Zezas A., Sell P., Kovlakas K., Bonfini P., Willner S. P., Ashby M. L. N., et al., 2020, *MNRAS*, 494, 5967
- Koyama Y., et al., 2013, *MNRAS*, 434, 423
- Kron R. G., 1980, *ApJS*, 43, 305
- Lackner C. N., Gunn J. E., 2012, *MNRAS*, 421, 2277
- Lauer T. R., et al., 2007, *ApJ*, 662, 808
- Lawrence A., Walker D., Rowan-Robinson M., Leech K. J., Penston M. V., 1986, *MNRAS*, 219, 687
- Lynden-Bell D., 1971, *MNRAS*, 155, 95
- Mahajan S., et al., 2019, *MNRAS*, 482, 560
- Maragkoudakis A., Zezas A., Ashby M. L. N., Willner S. P., 2014, *MNRAS*, 441, 2296
- Maragkoudakis A., Zezas A., Ashby M. L. N., Willner S. P., 2017, *MNRAS*, 466, 1192
- Maragkoudakis A., Zezas A., Ashby M. L. N., Willner S. P., 2018, *MNRAS*, 475, 1485
- Marino A., Bianchi L., Rampazzo R., Thilker D. A., Annibali F., Bressan A., Buson L. M., 2011, *ApJ*, 736, 154
- Mayer L., Mastropietro C., Wadsley J., Stadel J., Moore B., 2006, *MNRAS*, 369, 1021
- Moffat A. F. J., 1969, *A&A*, 3, 455
- Mould J. R., et al., 2000, *ApJ*, 529, 786
- Naab T., Johansson P. H., Ostriker J. P., 2009, *ApJ*, 699, L178
- Naab T., 2013, *IAUS*, 295, 340
- Oke J. B., Sandage A., 1968, *ApJ*, 154, 21
- Oser L., Ostriker J. P., Naab T., Johansson P. H., Burkert A., 2010, *ApJ*, 725, 2312
- Parry O. H., Eke V. R., Frenk C. S., 2009, *MNRAS*, 396, 1972
- Peng C. Y., Ho L. C., Impey C. D., Rix H.-W., 2010, *AJ*, 139, 209
- Peng Y., Maiolino R., Cochrane R., 2015, *Natur*, 521, 192
- Peterson B. M., 1997, *An Introduction to Active Galactic Nuclei*, Cambridge University Press
- Petrosian V., 1976, *ApJ*, 209, L1
- Protassov R., van Dyk D. A., Connors A., Kashyap V. L., Siemiginowska A., 2002, *ApJ*, 571, 545
- Rowan-Robinson M., 1968, *MNRAS*, 138, 445
- Saunders W., Rowan-Robinson M., Lawrence A., Efstathiou G., Kaiser N., Ellis R. S., Frenk C. S., 1990, *MNRAS*, 242, 318
- Saunders W., et al., 2000, *MNRAS*, 317, 55
- Schawinski K., et al., 2014, *MNRAS*, 440, 889
- Schechter P., 1976, *ApJ*, 203, 297
- Schmidt M., 1968, *ApJ*, 151, 393

- Schombert J., 2011, Systematic Bias in 2MASS Galaxy Photometry (arXiv:1107.1728)
- Serra P., et al., 2014, MNRAS, 444, 3388
- Simard L., 1998, ASPC, 145, 108
- Smith A. J., Loveday J., Cross N. J. G., 2009, MNRAS, 397, 868
- Springel V., et al., 2005, Natur, 435, 629
- Steinmetz M., Navarro J. F., 2002, NewA, 7, 155
- Stern D., et al., 2005, ApJ, 631, 163
- Strateva I., et al., 2001, AJ, 122, 1861
- Takeuchi T. T., Yoshikawa K., Ishii T. T., 2000, ApJS, 129, 1
- Tully R. B., Shaya E. J., Karachentsev I. D., Courtois H. M., Kocevski D. D., Rizzi L., Peel A., 2008, ApJ, 676, 184
- Vaughan S., Edelson R., Warwick R. S., Uttley P., 2003, MNRAS, 345, 1271
- White S. D. M., Rees M. J., 1978, MNRAS, 183, 341
- Willmer C. N. A., 1997, AJ, 114, 898
- Worthey G., 1994, ApJS, 95, 107
- Xu C. K., et al., 2006, ApJ, 646, 834
- Yagi M., et al., 2010, AJ, 140, 1814

**APPENDIX A: PRE-FITTING PROCEDURES****A1 Setting up GALFIT input**

Every  $\chi^2$  minimization-based algorithm, such as GALFIT, requires an initial parameter set from which to start mapping the  $\chi^2$  space determined by the model parameters. Appropriate choice of these initial values speeds-up the convergence to the the *best-fit* parameters and avoids local minima. In order to determine initial photometric and morphological parameters for the target galaxies (and any other source which is fitted simultaneously; see § 4.1), we used SExtractor v2.8.6 (Bertin & Arnouts 1996)<sup>14</sup>. This package performs source detection and deblending, and provides basic photometry for each source after estimating and subtracting the local background. A summary of the quantities of interest for this preliminary analysis, and the relevant SExtractor keys, are reported in Table A1 and described in further detail in Appendix A2.

We tuned the SExtractor configuration file, and especially the detection, analysis, and deblending thresholds, by extensively testing the software on the 2MASS images. For the whole SFRS data set we chose a single SExtractor setup, which represented the optimal compromise between the maximum number of detected sources and the limit at which the sub-components of the SFRS targets (e.g., arms, star-associations, etc.) start being deblended. For just ~10 problematic objects (contaminated by nearby stars or in close interacting pairs), we had to customize the SExtractor parameters in order to perform accurate photometry. One additional required setup parameter, used as an initial value for the SExtractor neural network which computes the stellarity index<sup>15</sup>, is an estimate of the seeing (or, equivalently, the stellar FWHM). We adopted the average FWHM of the stars within an 2MASS Atlas image and checked it was stable for different observation dates. In any case, this value was only used to perform the initial separation between point-like and extended sources. A deeper analysis of the PSF was anyway performed at the GALFIT fitting stage (see Appendix A4).

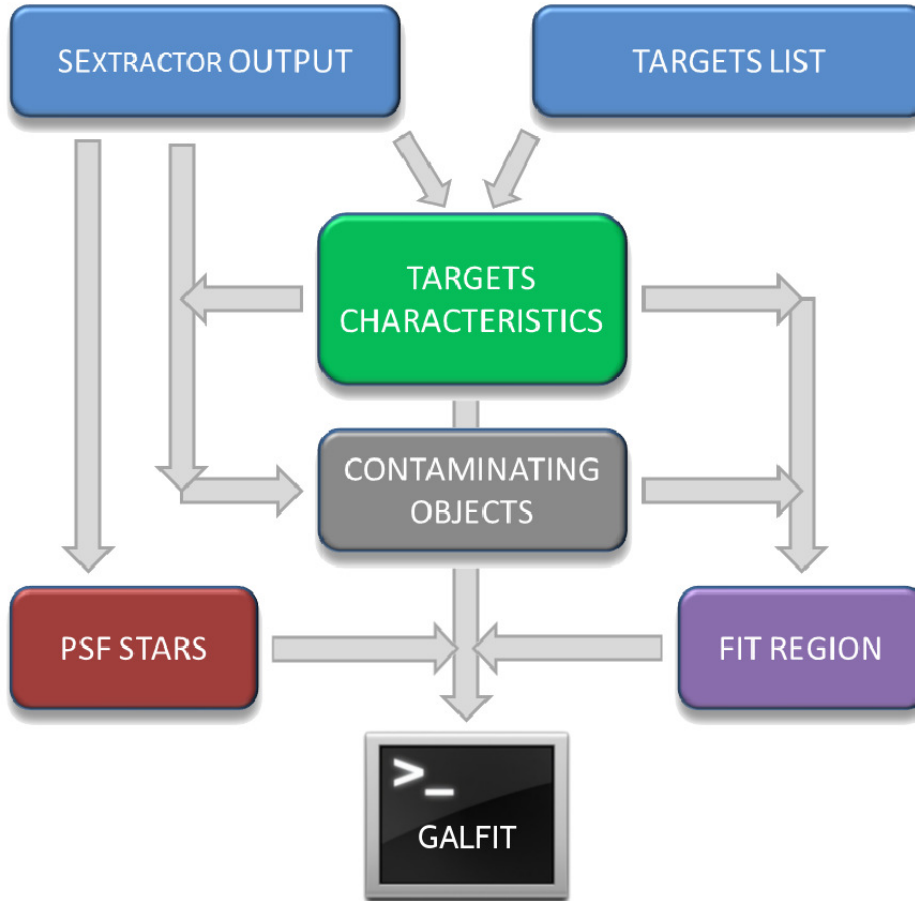


Figure A1: Flowchart representing the preparation of the GALFIT input. The SExtractor results were cross-matched against the input target list to associate each SFRS target to the corresponding Atlas image and to the relevant attributes produced by SExtractor. Contaminating objects (overlapping/blended) were identified based on their projected separation from the SFRS target. The best-quality stars were chosen as candidates to generate the model PSF required by the fit algorithm and to calculate the flux calibration. A fit region was cropped around the objects (or PSF stars) to be fit, based on their spatial extent, in order to speed up the fit calculations.

<sup>14</sup> [www.astromatic.net/software/sextractor](http://www.astromatic.net/software/sextractor)

<sup>15</sup> An estimate of the difference between the radial profile of an object and that of a point-like source.



The SExtractor results were processed as illustrated in Figure A1 in order to accomplish the following preparatory tasks.

- ▶ The SFRS targets were associated to their corresponding image files through a coordinate cross-match. In fact, given a list of targets and a list of images, our pipeline finds the correct association by comparing the WCS of the target with the FOV of the image.
- ▶ All the objects not associated with a SFRS target (i.e., overlapping/blended objects) were marked to be fit together with the target in order to remove their contribution. A source was labelled as “contaminating” if it laid within a circle centered on the SFRS target and of radius:

$$R = 5 \times (R_{obj}^{eff} + R_{target}^{eff}) , \quad (A1)$$

where  $R_{obj}^{eff}$  and  $R_{target}^{eff}$  are the effective radius of the object and the target, respectively. The multiplicative constant was chosen to account for the wings of the radial light distribution of the most extended sources. Point-like and extended contaminating sources were distinguished based on their SExtractor stellarity index (threshold set at CLASS\_STAR = 0.3), and they were fit with different models (see §4.1).

- ▶ Some of the stars were marked as candidates to be used for the generation of the model PSF required by the fit algorithm and to calculate the photometric zero-point of the image (“PSF stars”; see §B). We imposed several criteria for a star to be considered eligible: (a) the star could not be a contaminating object; (b) the star could not be close to the image borders in order to have sufficient area to estimate the local background; (c) stellarity index > 0.8; (d)  $0.7 \times FWHM_{PSF} < FWHM_{star} < 1.5 \times FWHM_{PSF}$ , where  $FWHM_{PSF}$  is the input estimate for the PSF FWHM (determined as discussed in A4); (e) axis ratio  $b/a > 0.8$ ; (f) the star had to be isolated, i.e., it could not be blended with other objects according to SExtractor.
- ▶ A “fit region” was cropped around the group of objects to be fit in order to speed up the fitting calculations. The size of this area (based on the effective radii of the objects) was designed to be as small as possible, while still guaranteeing complete coverage of the extended wings of the sources light profiles and a sufficient sampling of the background. Similarly, a fit region was cropped around each PSF star. Figure A2 (first panel on the left) shows an example of the source effective radii and fit regions for the SFRS targets NGC 4435 and NGC 4438.

Although we heavily relied on SExtractor for the initial photometry of the sources, we preferred not to use its background maps, which are significantly contaminated by the light of actual sources<sup>16</sup>. This implies a systematic bias in the estimation of the background noise, which inevitably leads to erroneous weighting of the data values (see §4.1) and ultimately biases or yields additional uncertainties on the fit parameters. Therefore, in order to achieve a more robust estimate of the background and its noise, we developed a technique which heavily masks all the sources before evaluating the sky statistics. To do so, we took advantage of the SExtractor “segmentation” maps: these are FITS images in which every pixel deemed part of a source is masked out, essentially creating a map of the pixels belonging to detected objects. We created a PERL script<sup>17</sup> which expands isometrically the border of each object in the segmentation image, leaving “unmasked” only the pixels associated with a “secure” background. In this analysis, we roughly tripled the number of masked pixels with respect to the SExtractor segmentation maps. By applying this conservative masking on the data image, we measured the fiducial background mean and root-mean-square (RMS). The background level so measured was held fixed along the fitting process in order to avoid known degeneracies with model parameters such as, e.g., the Sérsic index and effective radius (e.g., Graham et al. 1996).

A final remark regards the setup of the saturation level (used by SExtractor to reject bad pixels) and the camera gain (used by both SExtractor and GALFIT for noise statistics) for each image. In fact, those quantities are exposure-dependent, as they depend on the actual 2MASS telescope that performed the observation (either Mt. Hopkins, Arizona or Cerro Tololo, Chile). The 2MASS cameras were modified during the course of the observing operations, which started in 1997 and were completed in 2001, and the SFRS sources have been observed with either cameras. We obtained the proper gain value using the time evolution of the 2MASS  $K_s$ -band gains, available online<sup>18</sup>. As for the saturation levels, we used the median values of the 2MASS Saturation Threshold Maps<sup>19</sup>.

## A2 SExtractor measurements

In order to automate the choice of initial photometric and morphological parameters for the target galaxies (and any other source which is fitted simultaneously), we used SExtractor v2.8.6 (Bertin & Arnouts 1996). The SExtractor keys<sup>20</sup> corresponding to each measurement are listed in Table A1.

*Source equatorial coordinates* — Used to automatically identify which, among the input images, contains a given target. SExtractor uses the header WCS information to provide the equatorial coordinates of each object: these are the coordinates used for the “blind search” (Appendix A1).

*Pixel position of source within the image* — Used to locate a given target within a 2MASS Atlas image and define a fit area around the target (Appendix A1). SExtractor determines the pixel position of a source by evaluating its centroid within the isophotal boundary calculated according to the limiting  $S/N$  desired by the user. It also offers an equivalent measurement performed within a circular Gaussian “window”

<sup>16</sup> See e.g., <http://users.obs.carnegiescience.edu/peng/work/galfit/TOP10.html>

<sup>17</sup> Publicly accessible from: <https://paolobonfini.wordpress.com/2016/05/04/mask-borders-of-a-fits-image>

<sup>18</sup> Available at: [www.ipac.caltech.edu/2mass/releases/allsky/doc/sec6\\_8a.html](http://www.ipac.caltech.edu/2mass/releases/allsky/doc/sec6_8a.html)

<sup>19</sup> Available at: [www.ipac.caltech.edu/2mass/releases/allsky/doc/sec4\\_2.html](http://www.ipac.caltech.edu/2mass/releases/allsky/doc/sec4_2.html)

<sup>20</sup> For a detailed description of the SExtractor keys, please refer to the SExtractor manual, or to the “Source Extractor for Dummies” (Holwerda 2005)

(whose FWHM is equivalent to the half-light radius) intended to avoid the limitations which affect the isophotal boundaries (i.e., changes in the detection threshold, and azimuthal irregularities). We opted to use the “windowed” centroids, as suggested by [Bertin & Arnouts \(1996\)](#), due to their higher reliability.

*Source Flux* — Used to calculate first-guess object magnitude ([Appendix A1](#)). SExtractor offers flux measurements for a variety of apertures. We used for the isophotal-corrected aperture which is a circularization of the isophotal boundary (which is discontinuous because its profile follows a pattern defined by the pixel borders) based on the assumption of a symmetric Gaussian profile for the object. This aperture is intended to recover the flux lost in the wings of the object profile. Although an elliptical aperture would better estimate galaxian fluxes, the isophotal-corrected aperture applies particularly well to stars, which compose the vast majority of objects we had to fit with our pipeline. In any case, the flux measured in this way for the objects of interest is only the initial parameter in the GALFIT analysis, which will provide the ultimate photometry.

*Source size* — Used to define the size of fit area around the target ([Appendix A1](#)). We set the PHOT\_FLUXFRAC key to 0.5 in order to obtain the effective radius  $R_e$  of the target.

*Position Angle (P.A.) and axis ratio* — Used as initial orientation and elongation of the fit model.

*Object type* — Used to separate stars from extended objects in order to decide the relevant fit model ([Appendix A1](#)) and to produce the model PSF ([Appendix A4](#)). To each cluster of pixels above the desired “analysis threshold”, SExtractor attributes a “stellarity-index”, whose value varies between 1 (secure point-like source) and 0 (secure extended source).

*Data quality* — Used to select the best candidate stars to be combined in the production of the model PSF ([Appendix A4](#)). SExtractor flags any object affected by issues such as blending or data corruption (e.g., saturated pixels within the aperture, memory overflow, etc.). Stars presenting any of these flaws were excluded from the pipeline creating the model PSF.

SEXTRACTOR: KEYS OF INTEREST	
Quantity	SEXTRACTOR Key
R.A.	ALPHA_J2000
Dec	DELTA_J2000
X pixel position	XWIN_IMAGE
Y pixel position	YWIN_IMAGE
Flux	FLUX_ISOCOR
Source size	FLUX_RADIUS
P.A.	THETA
Axis ratio	ELONGATION
Object type	CLASS_STAR
Data quality	FLAGS

Table A1: List of SExtractor outputs used to derive first-guess fit parameters.

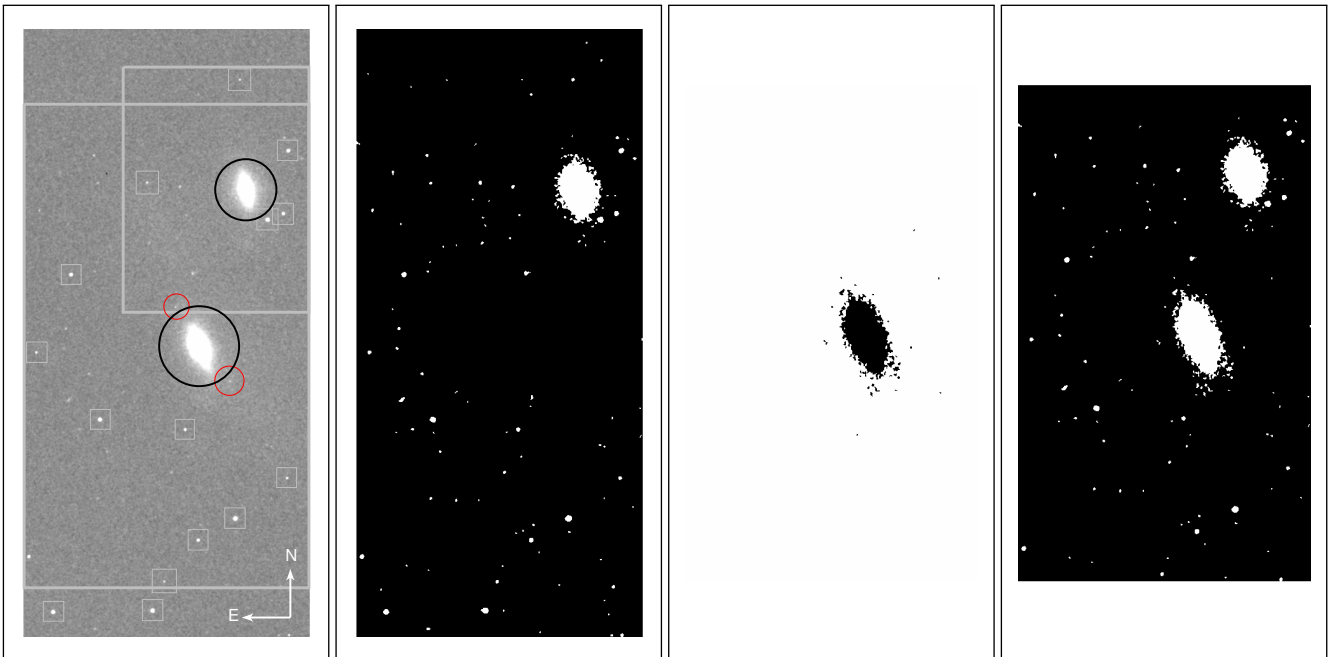


Figure A2: Results of the masking procedure for the SFRS target NGC 4438. *Left* — On a 2MASS  $K$ -band Atlas image we overplot the effective radii of the detected sources (black circles) and the fit regions (squares) as determined by the procedure described in [A1](#). This specific Atlas image contains two SFRS targets: NGC 4438 (center) and NGC 4435 (N-W), which are identified and processed simultaneously by the pipeline. Circles are centered on the source coordinates and have a radius equal to 5 times the sources’ effective radii as measured by SExtractor. Black circles mark the target of interest, while red circles mark contaminating objects. The fit of each target was performed only within the wide grey box enclosing the object. The smaller boxes identify the PSF stars and their fit region. *Center-left* — Mask image for NGC 4438: all targets but NGC 4438 and its contaminating objects are masked. *Center-right* — and *Right* — panels represent respectively the “negative mask” and the “negative background mask” for NGC 4438, which we used to select the best-model (see §5). The negative masks are smaller because they are defined only within the limits of the fitting region for a given object. In all masks, a white pixel defines a “masked” location, while a black pixel corresponds to a valid data point.

### A3 Mask creation

GALFIT allows the usage of pixel masks in order to “hide” the objects whose flux will not be accounted for in the fit: all the masked pixels are simply ignored. We created mask images by exploiting the SExtractor segmentation maps, in which clusters of connected pixels attributed to a specific detected object are grouped in patches. We modified these segmentation maps in order to mask the undesired sources within the fit regions.

At this stage, we also produced two “negative” masks for the objects to be fit and for the background to mark the areas over which we evaluated the fit residuals used for the selection of the *best-fit* model (Section 5). An example of the masks used for the SFRS target NGC 4438 is shown in Figure A2.

### A4 PSF creation

GALFIT adopts a PSF-fitting procedure which performs a convolution of the target model with the image PSF before evaluating the statistics of each fit iteration. Therefore, an accurate reproduction of the PSF profile is the most critical (and difficult) step in the fitting process. An ideal PSF is required to have high  $S/N$ , account for geometric distortions (e.g., ellipticity), and of course be at least Nyquist sampled.

In general, the 2MASS optical system guarantees a PSF FWHM  $< 2''$  across the whole  $512''$  field of view of the camera. Gradients along the CCD are further minimized (averaged) by the scanning technique (Beichman et al. 1998) and subsequent image combination (Section 3.2). Although the PSF along a 2MASS scan is fairly constant in standard observational conditions (Jarrett et al. 2000, Figure 5), it may vary between exposures due to thermal and atmospheric condition differences. For this reason, we had to define a PSF model for each observation independently.

Using as a model PSF a background-subtracted star from the native image is the simplest approach, but it does not always satisfy the required characteristics. Moreover, GALFIT is extremely sensitive to the PSF shape. PSFs derived from individual stars led to failed fits for the vast majority of the objects. On the other hand, a single *theoretical* PSF profile (e.g., Moffat) used in all data would not account for peculiar features such as diffraction rings and spikes, nor be representative of the PSF across the field or at different times. For these reasons, we decided to pursue a hybrid approach by modelling the best-quality stars in the field (“PSF stars”; see A1) and then combining these model PSFs to produce the final PSF for each image. First, we used GALFIT to fit all the PSF stars assuming a Moffat function (Moffat 1969), widely used to describe star profiles, plus a background component. Then, each background-subtracted model was re-projected onto a canvas 30 times the PSF FWHM, wide enough to include the PSF wings (while keeping the computational time within a reasonable limit). Smaller PSF canvas sizes resulted in evident truncations in the final target models. The pixel scale of these PSF images was set to match that of the native Atlas images in order to avoid the complications related to oversampling; no additional resolution is needed as the 2MASS PSF is already Nyquist sampled, its FWHM covering approximately 3.5 pixels. Finally, the normalized PSF images associated to the models characterized by the best  $\chi^2$  were median combined (using Swarp; Bertin et al. 2002) to create the adopted PSF image. This way we generated for each image a model PSF that is representative of the PSF shapes present across the field. We additionally compared our PSFs against the PSFs generated via PSF EXTRACTOR (Bertin 2011) as a combination of snap images of real stars in the field. Our PSFs — being constructed from a combination of “smooth” Moffat models — were marginally superior in that they were *not* presenting any artefact (due e.g., to bad pixels) which would ultimately reflect in the galaxy model.

Figure A3 shows the Moffat fits to the radial profiles of a sample of 1 000 randomly selected PSF stars. In the same figure, the FWHM of the stars is compared with the distribution of effective radii of the SFRS galaxies (as derived from the single Sérsic fits; see §4.1) to show that only a tiny minority of the targets are partially resolved. For a few fields, due to a lack of candidate PSF stars, the image PSF was substituted by one adopted from to another image, chosen to be the closest in time, with the obvious constraint that it should have been acquired by the same 2MASS telescope and camera.

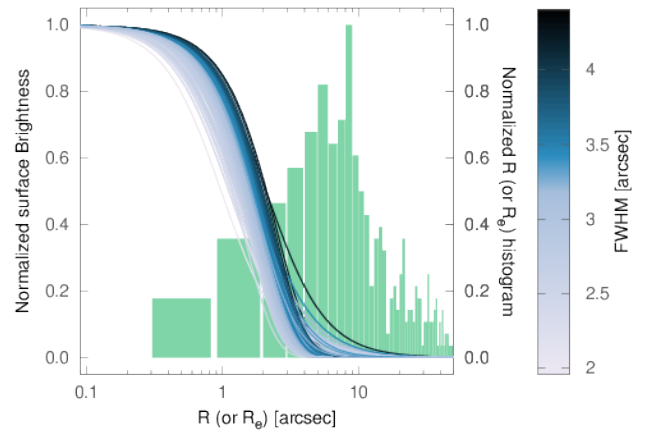


Figure A3: Comparison of the 2MASS seeing against the SFRS target sizes. The solid curves represent the Moffat profile fits to the surface brightness of 1 000 PSF stars randomly selected among the 2MASS Atlas images. The curves are normalized to a unit peak intensity and are color-coded by FWHM, with darker curves showing more extended profiles. The green histogram shows the distribution of effective radii ( $R_e$ ) of the SFRS galaxies, obtained through the fit of a single Sérsic model (as described in §4); the normalization is arbitrary.

## APPENDIX B: ZERO-POINTS, LUMINOSITIES, AND STELLAR MASS CALCULATION

The zero-point was derived by comparing the magnitudes resulting from the fit of the PSF stars in each image against the corresponding source flux densities published in the 2MASS-PSC (Cutri et al. 2003). We cross-correlated our PSF stars against the 2MASS-PSC sources encompassed by the field of an Atlas image, using a search radius of  $1''$  (which is  $\sim 2\sigma$  the centroid accuracy of the 2MASS catalog), selecting the matches with the minimum projected separation. Zero-points were separately calculated for each PSF star, using the following relation:

$$ZP^\star = mag^{2MASS} - mag^{GALFIT} \quad (B1)$$

$$\delta ZP^\star = \sqrt{(\delta mag^{2MASS})^2 + (\delta mag^{GALFIT})^2},$$

where  $mag^{2MASS}$  is the star flux in magnitude units in the 2MASS-PSC,  $mag^{GALFIT}$  is the measured, uncalibrated source intensity for each source (instrumental magnitude),  $\delta ZP^\star$  is the uncertainty on the zero-point estimated for the star, and  $\delta mag$  are the uncertainties of the 2MASS and GALFIT magnitudes.

The zero-point of a field ( $ZP$ ) was simply estimated as the weighted average of the zero-points  $ZP^\star$  of the stars within the image. The calculation of the uncertainty of the  $ZP$  (i.e.,  $\delta ZP$ ) required instead a more sophisticated approach. Although ideally one would calculate  $\delta ZP$  as the standard deviation of the  $ZP^\star$  of the stars in each field, the majority of the images offered fewer than 5 stars suitable to calibrate the zero-point (see selection criteria in Appendix A1), insufficient for this type of analysis. In order to evaluate  $\delta ZP$ , we instead studied the distribution of the zero-points of the whole 2MASS images sample (presented in Figure B1). The distribution is bimodal, with the peaks corresponding to the zero-points for the two 2MASS instruments (Mt. Hopkins, Arizona and Cerro Tololo/CTIO, Chile). Assuming that the variation of the 2MASS zero-points around the mean values is due only to photometric uncertainties, we fitted the distribution with two superimposed Gaussian components using the *Sherpa* package v4.2.1 (which is part of the CIAO tool suite v4.2). The uncertainties in the height of each bin were calculated using the Gehrels (1986) approximation (Equation 18).

The parameters of the *best-fit* model (overplotted in Figure B1) are reported in Table B1, where the error bars refer to the  $1-\sigma$  (68.3%) confidence bounds from the  $\Delta\chi^2$  projection for 1 interesting parameter. The FWHMs of the two components were used as a statistical estimate of the uncertainty of the zero-points: in particular, we attributed a  $\delta ZP$  equivalent to the FWHM of the model ‘‘Gaussian 1’’, and ‘‘Gaussian 2’’ (see Table B1) to all the images observed with the CTIO, and Mt. Hopkins instrument, respectively. Similarly, for the images without a sufficient number of stars to confidently estimate the  $ZP$ , we used the mean fit value of the gaussian corresponding to the relevant instrument.

Finally, the integrated magnitudes for each target, as well as the magnitudes for each model sub-component were converted to fluxes ( $\text{erg sec}^{-1} \text{cm}^{-2}$ ) using the flux-to-magnitude conversion:

$$F_K = \nu_K \times (f_{0,K} \times 10^{-0.4 \cdot M_K}) \times 10^{-23}, \quad (B2)$$

where  $f_{0,K}$  is the zero-magnitude zero point conversion value ( $666.7 \text{ Jy}$ )<sup>21</sup>,  $\nu_K$  ( $1.4 \times 10^{14} \text{ Hz}$ ) is the central wavelength of the  $K_s$ -band filter,  $M_K$  is the object (model sub-component) magnitude, and the term  $10^{-23}$  is the conversion factor from  $\text{Jy}$  to  $\text{erg s}^{-1} \text{cm}^{-2} \text{Hz}^{-1}$ . The  $K$ -band  $K$ -correction was performed following the prescriptions by Chilingarian, Melchior, & Zolotukhin (2010), where we used the 2MASS  $J - K$  color (Ashby et al. 2011, their Table 9) as a proxy for the galaxy spectrum. We derived the luminosities of the SFRS objects by converting their fluxes using the distances tabulated in Ashby et al. (2011).

Based on the mass-to-light ratio ( $M/L$ ) for a given stellar population, one can convert the  $K_s$ -band luminosity of a galaxy to its stellar mass. However, this conversion factor is a function of the age of the population, mainly through the non-linear dependence of the luminosity of individual stars on their mass ( $L \propto M^{3.5}$ ), and its metallicity. For example, the  $M/L$  changes by more than 10% when the assumed stellar age increases by 1 Gyr, and by more than 20% when the metallicity  $[\text{Fe}/\text{H}]$  increases by 0.5 dex. These figures are based on the evolutionary

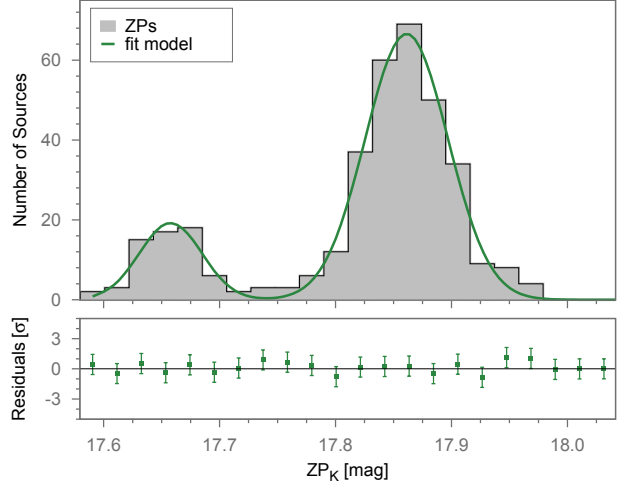


Figure B1: Distribution of the zero-points (binned in 0.02 mag bins) for the 2MASS Atlas images containing the SFRS targets, over which we plot the results of a double Gaussian fit (green line). The bottom panel shows the fit residuals in units of standard deviation.

FIT RESULTS FOR THE ZERO-POINT DISTRIBUTION			
Component	Amplitude	Peak [mag]	FWHM [mag]
Gaussian 1	$19.25^{+4.23}_{-4.09}$	$17.66^{+0.01}_{-0.01}$	$0.06^{+0.01}_{-0.01}$
Gaussian 2	$66.61^{+6.12}_{-6.00}$	$17.86^{+0.00}_{-0.00}$	$0.08^{+0.01}_{-0.01}$

$\chi^2_\nu = 0.38$ , 18 d.o.f. ( $P(Q\text{-value}) = 0.99\%$ )

Table B1: Fit results for the double Gaussian fit of the zero-point distribution (Figure B1).

<sup>21</sup> Available at: <http://www.ipac.caltech.edu/2mass/releases/allsky/faq.html#jansky>



models by [Worthey \(1994\)](#)<sup>22</sup>, where we assumed as central values a solar metallicity and a light-weighted age of  $\sim 2$  Gyr (appropriate for our star-forming galaxies; e.g., [Peng, Maiolino, & Cochrane 2015](#)) and adopted the default Salpeter initial mass function prescriptions.

As a first-order proxy of the age/metallicity of the stellar population, one can use its colour (e.g., [Bruzual & Charlot 2003](#)). In our analysis, we estimated the stellar mass of the galaxies (and of their sub-components) using the prescriptions of [Bell et al. \(2003\)](#), which provides mass-to-light ratios as a function of colour for several 2MASS and SDSS passbands. In particular, we used the formulation:

$$\frac{M}{M_{\odot}} = 10^{-0.273+(0.091 \times (u-r))} \times \frac{L_K}{L_{\odot}}, \quad (\text{B3})$$

where  $u$  and  $r$  are the corresponding SDSS model magnitudes (see §6.3),  $L_K$  is the target luminosity in  $K_s$ -band, and  $M_{\odot}$  and  $L_{\odot}$  are the solar mass and luminosity, respectively ( $M_{\odot} = 1.989 \times 10^{33}$  g,  $L_{\odot} = 4.97 \times 10^{32}$  erg s<sup>-1</sup>). The  $(u-r)$  SDSS colours for the SFRS galaxies (see Table D1) are based on their integrated SDSS photometry, therefore they reflect the average colour of the stellar content. For the calculation of the separate masses of the disk/bulge sub-components we adopted the disk/bulge colors we derived via 2D fitting of the SDSS-DR12 imaging, as discussed in §6.3.

### APPENDIX C: COMPLETENESS TEST

We verify the accuracy of the completeness correction evaluated in §7.2 by applying it to the construction of the  $60\mu\text{m}$  LF for the SFRS sample, which we produced following the same methodology as described in §7. Given our definition of completeness, the  $60\mu\text{m}$  SFRS LF is effectively the LF of the PSC<sub>z</sub> galaxies, which we compared against the PSC<sub>z</sub> LF derived by [Takeuchi, Yoshikawa, & Ishii \(2000\)](#). The two functions are shown in Figure C1 along with the reference LF of 2 818 IRAS selected galaxies by [Saunders et al. \(1990\)](#). The remarkable agreement between the curves confirms the reliability of our completeness correction.

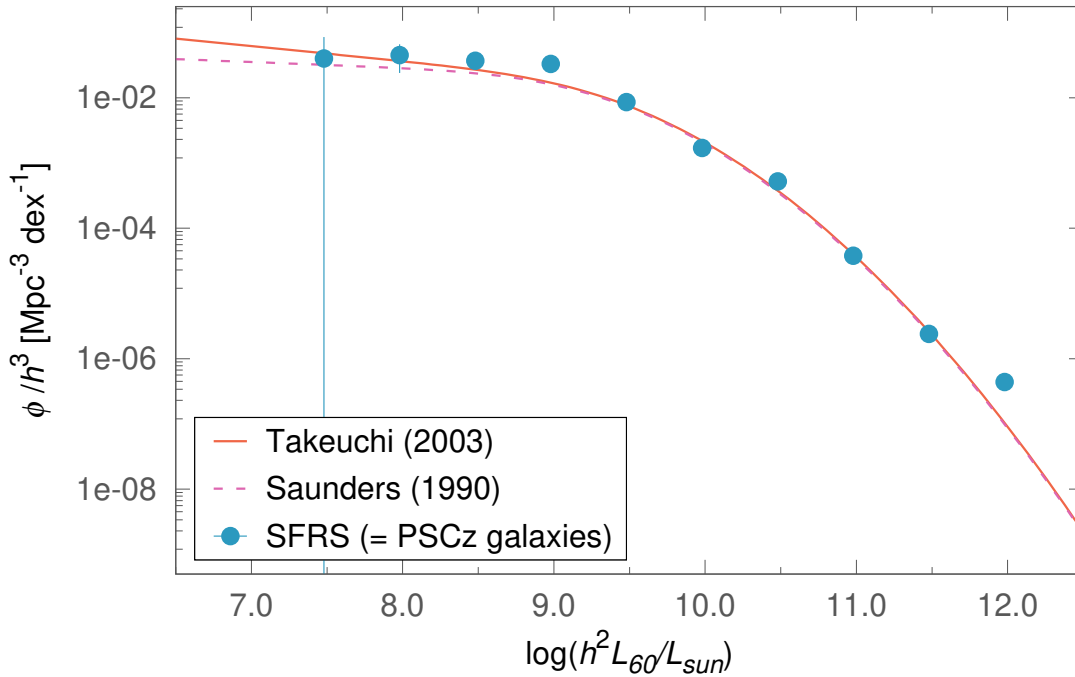
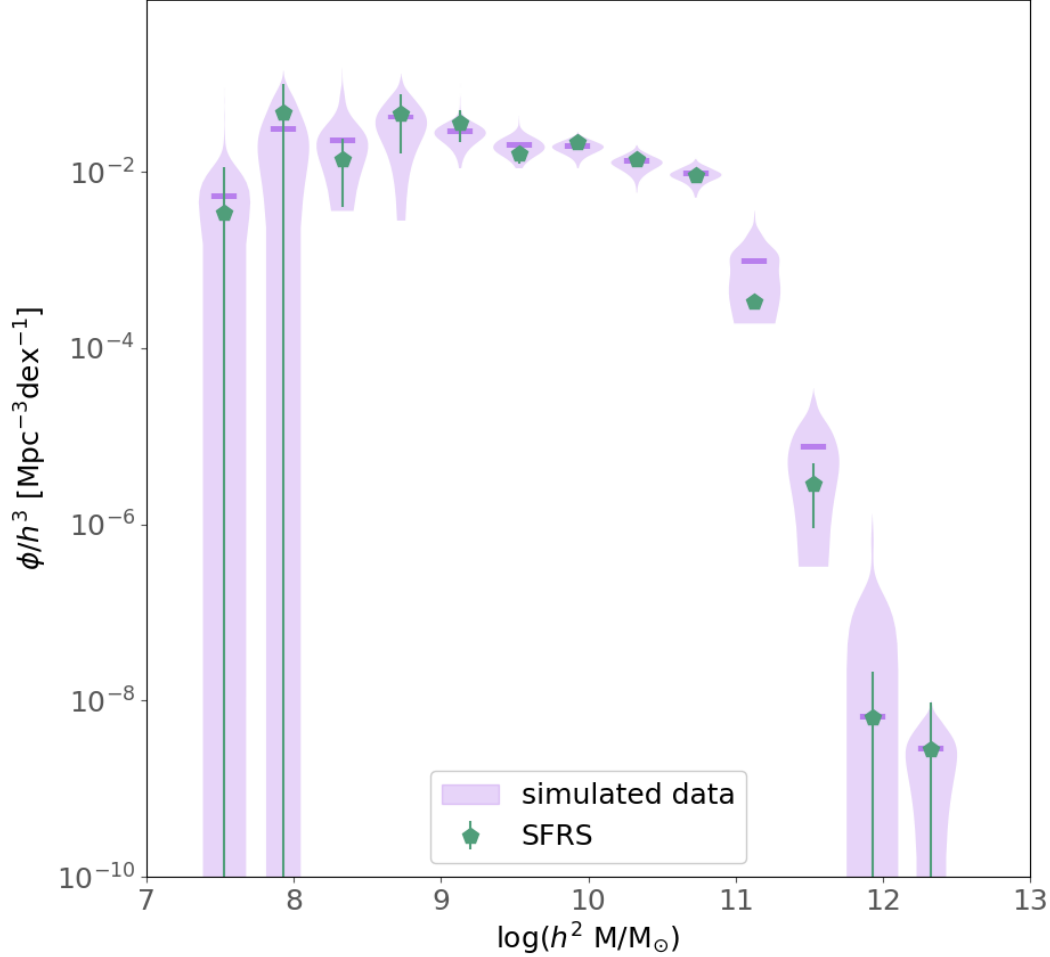


Figure C1: Comparison with published  $60\mu\text{m}$  PSC<sub>z</sub> LFs. The  $60\mu\text{m}$  LFs built from the SFRS sample by applying the completeness correction presented in §7.2 effectively corresponds to the LF of the galaxies within the PSC<sub>z</sub> catalogue (blue data points). The SFRS data shall be compared against the corresponding PSC<sub>z</sub> LF by [Takeuchi, Yoshikawa, & Ishii \(2000\)](#), solid curve). As a reference, the dashed curve shows the LF for the IRAS-selected galaxies of [Saunders et al. \(1990\)](#).

### APPENDIX D: MASS FUNCTION UNCERTAINTIES ASSESSMENT

The Poissonian uncertainties assumed in our MF (§7) represent a lower limit on the uncertainties. In addition, there are the following factors that may contribute to the uncertainties of the derived MF.

<sup>22</sup> Through the “Worthey model interpolation engine” applet [http://astro.wsu.edu/worthey/dial/dial\\_a\\_model.html](http://astro.wsu.edu/worthey/dial/dial_a_model.html)



**Figure D1.** MF derived from the Monte Carlo simulation described in Appendix D. The green diamond points and error bars represent the calculated SFRS MF as shown in Figure 13. The purple violins show the density distribution of the simulated values (estimated through a Gaussian kernel), while the thick horizontal bars indicate the median of the simulated values within each bin.

- Uncertainty in selecting the SFRS galaxies from the PSCz catalogue.* As a reminder, the SFRS galaxies were selected by first binning the PSCz in the three-dimensional space of IRAS 60  $\mu\text{m}$  luminosity and the two flux density ratios  $F_{100}/F_{60}$  and  $F_{60}/K_s$  and then selecting up to 10 galaxies from the PSCz galaxies in each 3D bin. The weight assigned to each SFRS galaxy is the number of PSCz galaxies it represents, i.e., number of PSCz galaxies in the bin divided by the number selected for the SFRS. (Refer to §2 and Ashby et al. 2011 for more details on the sample creation, including the bin definitions and how the numbers for each bin were chosen.) We therefore want to address the question: "if we had randomly chosen a different set of SFRS galaxies, how much different would the number counts in each mass bin and resulting MF be?".
- Uncertainties in the binning.* The SFRS bin boundaries could have been chosen differently, and the observational data used to assign PSCz galaxies to bins have finite uncertainties. We therefore want to address what would have happened with slightly different binning.
- Uncertainty in the mass measurement.* Errors in the mass measurements could shift SFRS galaxies to a different mass bin.

To assess how the above uncertainties propagate to the final MF, we performed a Monte-Carlo simulation. For each trial, we varied the galaxy number counts in the mass bins, the galaxy weights, and the galaxy masses and then calculated a new MF. Corresponding to the items above,

- the number of galaxies in each trial bin was varied from the actual number according to a Poisson distribution.
- the weights of the galaxies in each bin were varied according to a Poisson distribution of the weights, and then the trial total bin weight was equally re-distributed over the galaxies in the trial bin. The sum of the SFRS bin weights is by construction the number of PSCz galaxies

in the bin, and therefore a Poisson distribution should represent the uncertainties in counting PSCz galaxies. In this step we also ensured that the sum of all weights was within  $\pm 1$  of the number of galaxies in the PSCz, rejecting any trial that did not satisfy this condition.

- c) To account for the uncertainty in the mass measurement, the mass of each galaxy was sampled from a Gaussian distribution centered on the actual mass and with standard deviation equal to the mass uncertainty.

The Monte Carlo results of  $\sim 1\,000$  accepted trials are shown in Figure D1. The range among different trials should represent the uncertainties mentioned above. As can be seen, the ranges for most bins are comparable to the Poisson uncertainties with little systematic offsets. This gives confidence in the derived MF and its uncertainties. This strongly suggests that our derivation of the MF in §7.6 is robust against these additional uncertainty factors.

Table D1: List of SDSS (Data Release 12)  $u$ ,  $r$ , and 2MASS  $J$ ,  $H$ ,  $K$  magnitudes for the SFRS sample.  
 — The full version of this table is available online —

SFRS — 2MASS AND SDSS PHOTOMETRY										
SFRS ID	Target Name	ID	$u^{\ddagger}$	$r^{\ddagger}$	ID	$J^{\ddagger}$	$H^{\ddagger}$	$K^{\ddagger}$		
(1)	(2)	(3)	(4)	(5)	(6)	(7)	(8)	(9)		
1	IC486	SDSSJ080020.98+263648.8	15.856(0.006)	13.377(0.002)	XSC—08002097+2636483	11.514(0.020)	10.826(0.021)	10.496(0.028)		
2	IC2217	SDSSJ080049.73+273001.5	15.269(0.005)	13.838(0.002)	XSC—08004972+2730010	11.834(0.024)	11.186(0.027)	10.898(0.040)		
3	NGC2500	SDSSJ080153.17+504413.5	14.104(0.005)	12.263(0.002)	XSC—08015322+5044135	10.790(0.021)	10.160(0.030)	9.276(0.065)		
4	NGC2512	SDSSJ080307.84+232330.5	15.081(0.005)	12.865(0.002)	XSC—08030785+2323308	10.859(0.020)	10.117(0.026)	9.820(0.028)		
5	MCG6-18-009	SDSSJ080328.94+332744.5	15.502(0.006)	13.642(0.002)	XSC—08032897+3327444	11.803(0.034)	11.135(0.034)	10.763(0.040)		
6	MK1212	SDSSJ080705.51+270733.7	16.365(0.007)	14.588(0.002)	XSC—08070551+2707336	12.594(0.026)	11.995(0.032)	11.589(0.045)		
7	IRAS08072+1847	SDSSJ081006.99+183818.0	18.271(0.020)	15.590(0.003)	XSC—08100697+1838176	13.270(0.038)	12.684(0.059)	12.189(0.056)		
8	NGC2532	SDSSJ081015.17+335723.9	15.549(0.009)	12.983(0.002)	XSC—08101519+3357233	10.643(0.022)	10.004(0.029)	9.615(0.036)		
9	UGC4261	SDSSJ081056.21+364941.3	15.771(0.006)	14.984(0.003)	XSC—08105615+3649435	12.887(0.037)	12.291(0.056)	12.027(0.067)		
10	NGC2535	SDSSJ081113.48+251224.8	15.227(0.008)	12.980(0.002)	XSC—08111348+2512249	10.993(0.027)	10.341(0.029)	10.120(0.043)		
11	NGC2543	SDSSJ081257.92+361516.6	15.083(0.007)	12.514(0.002)	XSC—08125795+3615162	10.532(0.023)	9.745(0.026)	9.431(0.030)		
12	NGC2537	SDSSJ081314.69+455922.0	13.880(0.004)	12.318(0.002)	XSC—08131464+4559232	9.949(0.022)	9.366(0.025)	9.130(0.034)		
13	IC2233	SDSSJ081358.77+454441.9	20.296(0.052)	22.550(0.250)	XSC—08135890+4544317	11.463(0.032)	10.950(0.042)	10.754(0.062)		
14	IC2239	SDSSJ081406.79+235158.9	15.931(0.007)	13.527(0.002)	XSC—08140678+2351588	11.363(0.021)	10.687(0.025)	10.339(0.028)		
15	UGC4286	SDSSJ081416.47+182626.3	16.045(0.011)	13.570(0.002)	XSC—08141648+1826258	11.897(0.025)	11.175(0.033)	10.868(0.038)		
16	UGC4306	SDSSJ081736.78+352644.3	16.221(0.011)	13.585(0.002)	XSC—08173676+3526455	11.449(0.023)	10.660(0.024)	10.333(0.030)		
17	NGC2552	SDSSJ081919.17+500017.6	22.230(0.295)	20.584(0.047)	XSC—08192055+5000351	14.524(0.088)	13.859(0.122)	13.607(0.148)		
18	UGC4383	SDSSJ082334.21+212051.5	15.614(0.006)	13.892(0.002)	XSC—08233424+2120514	12.244(0.037)	11.575(0.040)	11.368(0.047)		
19	IRAS08234+1054	SDSSJ082607.85+104451.0	21.853(0.272)	18.768(0.014)	XSC—08260790+1044514	13.927(0.094)	13.053(0.086)	12.778(0.167)		
20	IRAS08269+1514	SDSSJ082945.19+150439.3	17.804(0.031)	15.671(0.005)	XSC—08294519+1504394	13.671(0.075)	12.934(0.089)	12.373(0.090)		
21	NGC2604	SDSSJ083323.13+293219.7	14.412(0.004)	13.363(0.002)	XSC—08332305+2932190	12.041(0.037)	11.422(0.050)	11.044(0.060)		
22	NGC2608	SDSSJ083517.33+282824.3	15.016(0.007)	12.838(0.002)	XSC—08351736+2828246	10.299(0.019)	9.611(0.023)	9.326(0.030)		
23	MK92	SDSSJ083539.96+462928.1	16.065(0.005)	14.632(0.002)	XSC—08353993+4629279	12.493(0.071)	11.797(0.066)	11.468(0.053)		
24	NGC2623	SDSSJ083824.01+254516.2	16.134(0.008)	13.802(0.002)	XSC—08382409+2545167	11.572(0.020)	10.808(0.025)	10.427(0.027)		
25	CGCG120-018	SDSSJ083950.75+230836.1	16.946(0.014)	14.502(0.002)	XSC—08395080+2308357	12.582(0.032)	11.803(0.038)	11.488(0.051)		
26	NGC2644	SDSSJ084131.84+045851.3	14.925(0.005)	13.184(0.002)	XSC—08413189+0458488	11.232(0.034)	10.646(0.043)	10.359(0.061)		
27	UGC4572	SDSSJ084537.85+365604.7	15.566(0.005)	13.276(0.002)	XSC—08453783+3656047	11.546(0.024)	10.896(0.023)	10.649(0.039)		
28	UGC4653	SDSSJ085354.62+350844.0	16.746(0.013)	14.370(0.002)	XSC—08535462+3508439	11.960(0.104)	11.150(0.040)	10.654(0.033)		
29	IRAS08512+2727	SDSSJ085416.77+271559.5	16.640(0.008)	14.837(0.002)	XSC—08541681+2715592	12.952(0.043)	12.392(0.069)	11.924(0.067)		
30	OJ287	SDSSJ085448.87+200630.6	16.573(0.007)	15.421(0.004)	XSC—08544889+2006307	13.503(0.039)	12.567(0.039)	11.768(0.032)		
...	...	...	...	...	...	...	...	...		
...	...	...	...	...	...	...	...	...		
...	...	...	...	...	...	...	...	...		

(1) SFRS target ID; (2) Galaxy name; (3) SDSS-DR12 ID; (4) SDSS  $u$  magnitude (SDSS *ugriz* filter set); (5) SDSS  $r$  magnitude (SDSS *ugriz* filter set); (6) 2MASS Extended Source Catalogue (XSC) or Point Source Catalogue (PSC) ID; (7) 2MASS  $J$ -band magnitude; (8) 2MASS  $H$ -band magnitude; (9) 2MASS  $K$ -band magnitude; (10) 2MASS modelMag;  $\ddagger$ : 2MASS-XSC values refer to the “extrapolated magnitudes”. (*J.ext*, *H.ext*, and *K.ext*; see §3.1).



Table D2: GALFIT model results for the SFRS sample.  
 — The full version of this table is available online —

SFRS TARGETS — GALFIT MODEL RESULTS																		
Target Name	Selected Model	Model Comp.	Sérsic $n$	$R$ ["]	Comp. $m_K$ [mag]	K-corr	Comp. $L_K$ [erg s <sup>-1</sup> ]	$(u-r)$ [mag]	Comp. $M/L$ [ $L_\odot/M_\odot$ ]	$M/L$ [ $L_\odot/M_\odot$ ]	Comp. $M$ [ $M_\odot$ ]	Total $M^\dagger$ [ $M_\odot$ ]	Decomp. Method	$B/T$	$D$ [Mpc]	Nuc. Class.	Weight	
(1)	(2)	(3)	(4)	(5)	(6)	(7)	(8)	(9)	(10)	(11)	(12)	(13)	(14)	(15)	(16)	(17)	(18)	(19)
IC2217	Sérsic + exDisk	Sérsic bulge	4.0	8.1	11.56±0.12	0.969	1.48e+43	2.48	0.897	0.720	2.67e+10	4.51e+10	GALFIT	0.473±0.125	7.61e+07	HII	13.2	
IC2217	Sérsic + exDisk	exDisk	—	5.9	11.44±0.07	0.969	1.65e+43	1.58	0.743	0.720	2.47e+10	4.51e+10	GALFIT	0.473±0.125	7.61e+07	HII	13.2	
NGC2500	Sérsic + psfAgn	Sérsic disk	1.8	89.1	8.51 ±0.04	0.980	9.63e+42	1.50	0.730	0.784	1.41e+10	1.52e+10	GALFIT	0.001±0.001	1.50e+07	LINER	4.2	
NGC2500	Sérsic + psfAgn	psfAgn bulge	—	—	16.07±0.13	0.980	9.12e+39	4.64	1.410	0.784	2.59e+07	1.52e+10	GALFIT	0.001±0.001	1.50e+07	LINER	4.2	
NGC2512	Sérsic + psfAgn	Sérsic disk	1.5	14.0	9.92 ±0.04	0.962	5.51e+43	2.11	0.830	0.849	9.20e+10	1.03e+11	GALFIT	0.089±0.009	6.93e+07	HII	7.4	
NGC2512	Sérsic + psfAgn	psfAgn bulge	—	—	12.45±0.04	0.962	5.36e+42	1.51	0.732	0.849	7.89e+09	1.03e+11	GALFIT	0.089±0.009	6.93e+07	HII	7.4	
MCG6-18-009	Sérsic	Sérsic mixed	5.6	8.8	10.49±0.04	0.924	1.76e+44	NA	NA	0.788	—	2.79e+11	C → B/T	0.204±0.054	1.64e+08	HII	1.5	
MK1212	Sérsic	Sérsic mixed	4.1	2.1	11.57±0.04	0.928	7.27e+43	NA	NA	0.774	—	1.13e+11	C → B/T	0.184±0.049	1.73e+08	HII	7.4	
IRAS08072+1847	Sérsic + psfAgn	Sérsic disk	2.0	1.7	12.58±0.06	0.957	4.94e+42	2.59	0.918	0.935	9.12e+09	1.31e+10	GALFIT	0.290±0.077	7.08e+07	SN	8.1	
IRAS08072+1847	Sérsic + psfAgn	psfAgn bulge	—	—	13.55±0.10	0.957	2.02e+42	1.68	0.758	0.935	3.08e+09	1.31e+10	GALFIT	0.290±0.077	7.08e+07	SN	8.1	
NGC2532	Sérsic + psfAgn	Sérsic disk	1.2	18.8	9.85 ±0.04	0.959	7.35e+43	2.04	0.818	0.913	1.21e+11	1.47e+11	GALFIT	0.077±0.009	7.76e+07	HII	5.0	
NGC2532	Sérsic + psfAgn	psfAgn bulge	—	—	12.55±0.04	0.959	6.11e+42	2.06	0.821	0.913	1.01e+10	1.47e+11	GALFIT	0.077±0.009	7.76e+07	HII	5.0	
NGC2535	Sérsic + psfAgn	Sérsic disk	1.2	23.8	10.06±0.04	0.979	3.90e+43	1.70	0.762	0.854	5.98e+10	7.14e+10	GALFIT	0.065±0.006	6.16e+07	HII	5.5	
NGC2535	Sérsic + psfAgn	psfAgn bulge	—	—	12.96±0.04	0.979	2.70e+42	2.36	0.875	0.854	4.75e+09	7.14e+10	GALFIT	0.065±0.006	6.16e+07	HII	5.5	
NGC2543	Sérsic + psfAgn	Sérsic disk	3.5	43.1	9.04 ±0.04	0.982	1.82e+43	2.42	0.886	0.914	3.24e+10	3.51e+10	GALFIT	0.043±0.010	2.63e+07	HII	12.1	
NGC2543	Sérsic + psfAgn	psfAgn bulge	—	—	12.41±0.04	0.982	8.18e+41	2.08	0.825	0.914	1.36e+09	3.51e+10	GALFIT	0.043±0.010	2.63e+07	HII	12.1	
NGC2537	Sérsic	Sérsic disk	0.3	22.5	9.24 ±0.04	0.996	5.00e+42	2.01	0.813	0.740	8.18e+09	7.44e+09	GALFIT	0 ±0	1.50e+07	HII	3.2	
IC2233	Sérsic	Sérsic disk	1.0	50.1	10.73±0.04	0.998	1.06e+42	2.01	0.813	0.333	1.73e+09	7.09e+08	GALFIT	0 ±0	1.37e+07	HII	1.0	
IC2239	Sérsic + psfAgn	Sérsic disk	3.5	7.3	10.41±0.04	0.955	5.68e+43	2.37	0.876	0.883	1.00e+11	1.15e+11	GALFIT	0.123±0.041	8.85e+07	HII	13.2	
IC2239	Sérsic + psfAgn	psfAgn bulge	—	—	12.54±0.06	0.955	7.98e+42	2.44	0.889	0.883	1.43e+10	1.15e+11	GALFIT	0.123±0.041	8.85e+07	HII	13.2	
UGC4286	Sérsic + exDisk	Sérsic bulge	4.0	1.1	12.97±0.09	0.961	3.73e+42	4.09	1.257	0.896	9.43e+09	4.44e+10	GALFIT	0.151±0.136	7.35e+07	HII	3.0	
UGC4286	Sérsic + exDisk	exDisk	—	7.4	11.10±0.04	0.961	2.09e+43	1.89	0.792	0.896	3.33e+10	4.44e+10	GALFIT	0.151±0.136	7.35e+07	HII	3.0	
...	...	...	...	...	...	...	...	...	...	...	...	...	...	...	...	...	...	...
...	...	...	...	...	...	...	...	...	...	...	...	...	...	...	...	...	...	...
...	...	...	...	...	...	...	...	...	...	...	...	...	...	...	...	...	...	...

(1) Galaxy name; (2) Selected model (see definition in §4.1); (3) Selected model component (see definition in §4.1); (4) Physical interpretation of component; (5) Sérsic index; (6) Effective radius (for Sérsic), or scale height (for exDisk); (7) Component  $K$ -band magnitude (Vega system); (8)  $K$  correction factor; (9) Component  $K$ -band luminosity; (10) Component color form our decomposition (the global galaxy color is reported in Table D1); (11) Component mass-to-light ratio; (12) Galaxy mass-to-light ratio; (13) Component mass; (14) Total mass<sup>†</sup> (omitting AGN light, if any); (15) Decomposition method: labelled as “GALFIT” in case it was obtained through 2D fitting, or “C → B/T” in case it was derived using the concentration index (see §6.2); (16) Bulge-to-total ratio; (17) Distance from Ashby et al. (2011); (18) Nuclear classification by Maragkoudakis et al. (2018); (19) Galaxy representativeness weight from Ashby et al. (2011). If multiplied by a constant factor of 6.7, a weight provides the number of galaxies that the SFRS target represents in the PSCz catalogue (see Ashby et al. 2011 for details).

<sup>†</sup>NOTE: Because a different  $M/L$  is used for bulge, disk, and whole galaxy, the masses of the sub-components do *not* necessarily sum up to the total mass.